

## ELEMENTS OF RARE EARTH MAGNETISM

The purpose of this introductory chapter is to describe in a synoptic way those features of rare earth magnetism which provide the foundation for the rest of the book. Since this material is presented in the form of a survey, it does not claim to be as systematic and complete as the later chapters. Consequently, it may be necessary for those who are unfamiliar with the rare earths and their magnetism to find further details in the original articles and reviews to which we shall refer, even though we have attempted to present a reasonably self-contained account. We shall also frequently refer forward to later sections for a more exhaustive treatment of some of the topics which are cursorily introduced here. We hope however that the information we have collected together will also provide a useful summary for those who have some familiarity with the subject.

We set the scene with a brief history of the field, outlining what we regard as the major advances. Even though we have striven to do justice to at least the majority of the important contributions, our viewpoint should not necessarily be considered as particularly objective. The magnetism of the rare earths has its origin in the angular momenta of the  $4f$  electrons in the atoms and we therefore describe in Section 1.2 their electronic structure and magnetic characteristics, introducing such essential ideas as *density-functional theory*, *Russell-Saunders coupling* and *Hund's rules*, and outlining how to calculate the *magnetic moment* of an unfilled subshell. We condense these atoms into a metal in Section 1.3, which is concerned with the description of the *conduction-electron gas* and its influence on the *structural properties*. A physically transparent method for determining the electronic structure is outlined, and the way in which the *band structure* is built up from its constituent parts is described and illustrated, using the concepts of *canonical bands* and *potential parameters*. The nature of the  $4f$  states in the metals, and the occurrence of  $4f$  bands in Ce and its compounds, are briefly discussed. Our experimental knowledge of the electronic structure, and particularly of the *Fermi surface*, is summarized. The way in which the conduction electrons determine the *atomic volume* and *crystal structure* is explained, and the individual contributions of the different  $l$ -states described. In Section 1.4, the *magnetic interactions* are presented, both the *single-ion* terms resulting from the *crystal fields* and the *two-ion* coupling via

*indirect exchange* and other mechanisms. The *magnetoelastic effects*, due to the coupling between the lattice strains and the magnetic moments, are also discussed. The manner in which these interactions and the characteristics of the  $4f$  electrons combine to determine the magnetic properties of the metals is described in the last section. The observed *magnetic structures* of the heavy rare earths are presented and their occurrence under different circumstances discussed. Some features of the structures and their temperature dependence are described in terms of an elementary *mean-field theory*. The magnetism of the light rare earths is then briefly treated and the importance of the crystal fields emphasized. The effect of a *magnetic field* on the magnetic structures is mentioned, and the factors which determine the *magnetic anisotropy* discussed. Finally, the way in which *magnetostriction* can change the crystal symmetry and influence the magnetic structure is illustrated.

### 1.1 A brief history

The quantum theory of magnetism was first placed on a sound footing in 1932 by J.H. Van Vleck in his classic monograph *The Theory of Electric and Magnetic Susceptibilities*. In it, he extended the calculations of the magnetic susceptibilities of isolated rare earth ions, which had been performed by Hund (1925), to encompass the anomalous cases of Eu and Sm, which have low-lying multiplets, giving rise to *Van Vleck paramagnetism*. He was thus able to obtain good agreement with experiment over the whole series from La to ‘Casseiopaium’ (now Lu). The study of the metallic elements began in earnest when Urbain, Weiss, and Trombe (1935) discovered the *ferromagnetism* of Gd. Klemm and Bommer (1937) determined the *paramagnetic Curie temperatures* of the heavy rare earths and Néel (1938) showed that, in the presence of strong spin–orbit coupling on the ion and an interionic exchange interaction between the spins, these should be proportional, as observed, to  $(g - 1)^2 J(J + 1)$ . This later became known as the *de Gennes factor*.

Very little work was done on the rare earths during the war, but immediately afterwards F.H. Spedding, at Iowa State University, resumed his programme of producing the pure elements, and by the early 1950s relatively large quantities had become available. One of the first fruits of this programme was the extension of physical measurements to the light rare earths, when Parkinson, Simon, and Spedding (1951) detected a number of anomalies of magnetic origin in the *heat capacity*. Just previously, Lawson and Tang (1949) had showed that the  $\gamma$ – $\alpha$  phase transition in Ce, which can be induced either by pressure or cooling, resulted in no change of the fcc symmetry, but a substantial reduction of the lattice parameter. Zachariasen and Pauling independently ascribed this shrinking to the transfer of the localized  $4f$  electron to the conduc-

tion band, the so-called *promotional model*. Extensive measurements were carried out on polycrystalline samples of all the stable lanthanides through the 1950s, and summarized by Spedding, Legvold, Daane, and Jennings (1957) at the close of this early period of rare earth research. Of particular significance, in the light of later developments, was the observation of extra magnetic neutron-diffraction peaks in polycrystalline Er by Koehler and Wollan (1955).

The disparate theoretical components which were later brought together to form the *standard model* of rare earth magnetism were also formulated in the 1950s. Zener (1951) suggested that localized moments could be coupled together by an *indirect exchange* through the medium of the conduction electrons, and Ruderman and Kittel (1954) calculated this coupling quantitatively for nuclear moments embedded in a free-electron gas. Kasuya (1956) and Yosida (1957) extended the treatment of this *RKKY interaction* to localized electronic moments. Stevens (1952) invented his method of *operator equivalents*, which was of decisive importance for a satisfactory treatment of the crystal fields. Mason (1954) formulated a theory of *magnetoelastic effects*, while Zener (1954) showed how to calculate the temperature dependence of the magnetic anisotropy.

The classical period of rare earth magnetism was heralded by the publication of the *magnetization* measurements on monocrystalline Dy by Behrendt, Legvold, and Spedding (1957). The fabrication of single crystals of all the heavy rare earths followed successively, and their bulk magnetic properties were studied at Iowa State by Legvold and his students. They were also made available to Koehler and his colleagues at Oak Ridge for *neutron-diffraction* measurements, which revealed what he later described as ‘a panoply of exotic spin configurations’. By the time of the First Rare Earth Conference at Lake Arrowhead, California in October 1960, both the magnetic susceptibilities and structures had been extensively investigated. The papers of Legvold (1961) and Koehler, Wollan, Wilkinson, and Cable (1961) summarized the remarkable progress which had been made by that time.

Theoretical developments lagged little behind. Almost simultaneously with the observation of the *helical structure* in Dy, Enz (1960) showed that the magnetization curves implied such a structure, and pointed out the importance of magnetoelastic effects in inducing the transition to the ferromagnetic phase. Niira (1960) successfully interpreted the magnetization of Dy in the ferromagnetic phase by calculating the *spin-wave spectrum* of an anisotropic magnet, showing that a finite energy is required to create a long-wavelength excitation. This *energy gap* gives rise to an exponential decrease of the magnetization at low temperatures. Elliott (1961) considered the magnetic structures of the

heavy rare earths and their temperature dependences, utilizing a phenomenological *molecular-field model*. A similar approach was taken by Miwa and Yosida (1961), while Nagamiya, Nagata, and Kitano (1962) calculated the effect of a magnetic field on some of these structures, showing that a *fan* structure may exist between the helix and the ferromagnet. In these papers, the standard model first attained a coherent formulation.

The transport properties, particularly the *electrical resistivity*, were elucidated in the same period. De Gennes (1958) considered the *magnetic disorder scattering*, showing that it is proportional to the de Gennes factor in the paramagnetic phase, while Kasuya (1959) gave a very complete discussion of the same subject, including not only the paramagnetic phase but also scattering by spin waves and rare earth impurities. The first resistivity measurements on single crystals were made on Er by Green, Legvold, and Spedding (1961). The unusual temperature dependence of the resistance in the *c*-direction was explained by Mackintosh (1962) as a consequence of the incommensurable magnetic ordering, leading to *magnetic superzones*. Miwa (1963) and Elliott and Wedgwood (1963) made calculations of the magnitude of this effect, using the free electron model, which were in semi-quantitative agreement with the experimental results. Mackintosh (1963) pointed out that the spin-wave energy gap should also give rise to an exponential increase in the magnetic scattering at low temperature and deduced that the gap in Tb is about 20 K, a value later substantiated by direct measurements.

Until this time, the conduction electrons in the rare earths had been described by the *free-electron model*, but Dimmock and Freeman (1964) demonstrated that this simplification was unjustified when they calculated the *band structure* of Gd by the APW method. The conduction electrons were found to be largely *d*-like, as in the transition metals, and the Fermi surface far from spherical. At that time, single crystals of the purity required to allow conventional Fermi surface experiments were unavailable, so Gustafson and Mackintosh (1964) employed *positron annihilation*, initially in polycrystalline samples. Their most striking observation was that the number of *4f* electrons in Ce does not change greatly at the  $\gamma$ - $\alpha$  transition, in contradiction to the promotional model, and hence to the standard model. Later measurements on single crystals of the heavy rare earths showed that the conduction electrons are indeed far from free electron-like, and the experimental results could be well accounted for by relativistic APW calculations (Williams, Loucks, and Mackintosh 1966).

As the ground-state properties of the rare earth metals became progressively clarified, interest turned towards the *magnetic excitations*. Niira's pioneering theoretical work was followed by the calculation of

the spin-wave *dispersion relations* in a variety of heavy-rare-earth magnetic structures by Cooper, Elliott, Nettel, and Suhl (1962). The first observations of spin waves by *inelastic neutron scattering* were made at Risø by Bjerrum Møller and Houmann (1966), who obtained rather complete dispersion relations for Tb at 90 K. During the following years, Bjerrum Møller and his colleagues performed a series of experiments which revealed many novel phenomena, including the temperature- and field-dependence of the *magnon energies*, allowing the deduction of the exchange and its anisotropy, and crystal-field and magnetoelastic parameters. Magnons in the incommensurable helical phase, including *phason* excitations at long wavelengths, were also observed, as was the interaction of magnons with each other, with the conduction electrons, and with phonons, including coupling through a new mechanism involving the spin-orbit interaction of the conduction electrons, explained by Liu (1972a).

Callen and Callen (1963) further developed the theory of *magnetostriction*, putting it in the form used by Rhyne and Legvold (1965a) to interpret their pioneering measurements on single crystals. Callen and Callen (1965) also generalized the treatment of the temperature dependence of crystal-field and magnetoelastic parameters. Cooper (1968a,b) considered in detail the role of the magnetoelastic effects in the helical-ferromagnetic transition, and included them in calculations of the spin-wave energies. Turov and Shavrov (1965) had earlier proposed that, since the magneto-strain cannot follow the precession of the moments in a spin wave, the energy gap should not vanish when the hexagonal anisotropy is cancelled by an external magnetic field. This *frozen lattice* effect was observed by Nielsen, Bjerrum Møller, Lindgård, and Mackintosh (1970). In the late 1960s, the availability of separated isotopes allowed spin-wave measurements at Oak Ridge on a number of the heavy rare earths which, because of neutron absorption in the natural state, could otherwise only be studied with great difficulty. Of particular interest were experiments on the isotropic ferromagnet Gd, in which the *magnetic form factor* was studied by Moon and Koehler (1971) and the spin waves by Koehler, Child, Nicklow, Smith, Moon, and Cable (1970), and the clear evidence for a large *exchange anisotropy* in the *conical phase* of Er (Nicklow, Wakabayashi, Wilkinson, and Reed 1971a).

With the increasing understanding of the magnetic behaviour of the heavy rare earths, it was natural that attention began to turn to the lighter metals. Moon, Cable, and Koehler (1964) began what was destined to become a long-lasting study by a number of groups of the magnetic structure of Nd, and Cable, Moon, Koehler, and Wollan (1964) found indications of antiferromagnetic ordering in polycrystalline Pr. Bleaney (1963) had earlier shown that the crystal-field ground states

in Pr should be singlets, and in such *singlet ground-state systems* no magnetic ordering should occur unless the exchange exceeds a critical value. Johansson, Lebeck, Nielsen, Bjerrum Møller, and Mackintosh (1970) could indeed detect no signs of magnetic ordering at 4.2K in monocrystalline Pr. Shortly afterwards, the crystal-field excitations, or *magnetic excitons*, were observed by Rainford and Houmann (1971) and, on the basis of these results, Rainford (1972) proposed a crystal-field level scheme which is very close to that accepted today.

The achievements of the classical period were summarized in the compendium on the *Magnetic Properties of Rare Earth Metals*, edited by R.J. Elliott, which was published in 1972 and, in a sense, also signalled the end of this period. In the modern era, the principles which had been established by the early 1970s have been applied to attaining a deeper and more complete understanding of the elements, even though the primary interest has increasingly turned towards rare earth compounds and alloys. For example, the magnetic interactions in the exchange-dominated system Tb were studied in exhaustive detail with inelastic neutron scattering by Jensen, Houmann, and Bjerrum Møller (1975). The crystal-field dominated system Pr was subjected to a similarly careful investigation by Houmann, Rainford, Jensen, and Mackintosh (1979) and, from his analysis of these results, Jensen (1976a) concluded that Pr could be induced to order antiferromagnetically either by the application of a modest *stress* or, through the *hyperfine interaction*, as first proposed by Murao (1971), by cooling to about 40 mK. The former effect was observed by McEwen, Stirling, and Vettier (1978) while magnetic ordering at very low temperatures had been inferred from heat-capacity measurements by Lindelof, Miller, and Pickett (1975). However, the controversy surrounding this phenomenon was only finally settled by the unambiguous observation of magnetic ordering by neutron diffraction (Bjerrum Møller, Jensen, Wulff, Mackintosh, McMasters, and Gschneidner 1982). The effects of the crystal field alone were studied by Touborg and Høg (1974), by dissolving small amounts of the magnetic rare earths in Sc, Y, and Lu and determining the crystal-field level scheme through susceptibility measurements, in conjunction with inelastic neutron scattering (Rathmann and Touborg 1977).

Efforts to increase the purity of rare earth samples were rewarded by the observation of the *de Haas-van Alphen (dHvA) effect* in Gd by Young, Jordan, and Jones (1973) and the subsequent detailed elucidation of its Fermi surface, which could be satisfactorily accounted for by band structures calculated with the inclusion of the exchange splitting between up- and down-spin levels. More recently, the careful study of the dHvA effect in paramagnetic Pr by Wulff, Lonzarich, Fort, and Skriver (1988) has confirmed the success of the band model in describ-

ing the conduction electrons, and given extensive information on their interaction with the  $4f$  electrons.

The electronic structure of Ce has been of continued interest. Johansson (1974) elaborated the suggestion of Gustafson, McNutt, and Roellig (1969) that  $\alpha$ -Ce is a *4f-band metal*, and Glötzel (1978) and others have further explored this model by band structure calculations. Single crystals of  $\alpha$ -Ce suitable for dHvA experiments are extremely difficult to prepare, but Johanson, Crabtree, Edelstein, and McMasters (1981) have studied the related compound CeSn<sub>3</sub>, observing the  $4f$  character of the electrons at the Fermi surface. *Photoemission experiments* by Wieliczka, Weaver, Lynch, and Olson (1982) and Mårtensson, Reihl, and Parks (1982) proved highly informative in exploring the electronic structure of Ce. This work reflects the intense interest in the 1980s in the problem of non-integral  $4f$  occupancy, which gives rise to a variety of phenomena subsumed under the description *mixed-valent* behaviour, the most striking of which is the huge electronic heat capacity and associated effective masses measured in *heavy-fermion materials*. The discovery of *superconductivity* in CeCu<sub>2</sub>Si<sub>2</sub> by Steglich, Aarts, Bredl, Lieke, Meschede, Franz, and Schäfer (1979) stimulated a major effort in studying lanthanide and actinide heavy-fermion systems, and underlined the significance of the earlier observation of superconductivity in Ce under pressure by Probst and Wittig (1975).

The properties of itinerant  $4f$  electrons have predominantly been studied through rare earth compounds. Indeed the main thrust of the rare earth research programme has recently been towards understanding *compounds and alloys*, which are generally beyond the scope of this book, but which may nevertheless be largely understood in terms of the principles which we shall present. However, as will be discussed in later sections, there still remain a number of problems in the elements which await and occasionally obtain a solution. For example, the essential features of the classic puzzle of the magnetic structure of Nd have been clarified by McEwen, Forgan, Stanley, Bouillot, and Fort (1985). Gibbs, Moncton, D'Amico, Bohr, and Grier (1985) have re-examined the configurations of the moments in Ho and other heavy rare earths, using a combination of *synchrotron radiation*, which shows promise for very high-resolution structural studies, and neutron diffraction. They utilized the concept of *spin slips* to explain their results, and hence refocused attention on *commensurable magnetic structures*, which had originally been studied by Koehler, Cable, Wilkinson, and Wollan (1966). Initial studies of the excitations of such structures were performed by Larsen, Jensen, and Mackintosh (1987), who thereby explained the long-standing mystery of the stability of the cone structure in Ho at low temperatures. Other unexplained features of the neutron diffraction patterns from Ho

were accounted for by Jensen and Mackintosh (1990), who showed that intermediate structures, which they named *helifans*, could be stabilized by a magnetic field.

A new field of endeavour has been opened by the fabrication of *multilayers* of different species of rare earths and the study of their properties by Majkrzak, Cable, Kwo, Hong, McWhan, Yafet, Waszczak, and Vettier (1986), and by Salamon, Sinha, Rhyne, Cunningham, Erwin, Borchers, and Flynn (1986). The size of the teams working on a number of these modern projects in rare earth research reflects the technical complexity of the problems now being tackled, and no doubt also the collaborative spirit of the age.

## 1.2 Rare earth atoms

The starting point for the understanding of the magnetism of the rare earths is the description of the electronic states, particularly of the  $4f$  electrons, in the atoms. The wavefunction  $\Psi(\mathbf{r}_1\sigma_1, \mathbf{r}_2\sigma_2, \dots, \mathbf{r}_Z\sigma_Z)$  for the electrons, which is a function of the space and spin coordinates  $\mathbf{r}$  and  $\sigma$  of the  $Z$  electrons which constitute the electronic charge cloud ( $Z$  is the atomic number), is determined for the stationary state of energy  $E$  from the Schrödinger equation

$$\mathcal{H}\Psi = E\Psi, \quad (1.2.1)$$

where the non-relativistic Hamiltonian operator is

$$\mathcal{H} = -\frac{\hbar^2}{2m} \sum_i^Z \nabla_i^2 + \frac{1}{2} \sum_{ij}^Z \frac{e^2}{|\mathbf{r}_i - \mathbf{r}_j|} + \sum_i^Z v_{\text{ext}}(\mathbf{r}_i) \quad (1.2.2)$$

and, in the case of an atom, the ‘external’ potential  $v_{\text{ext}}(\mathbf{r})$  is just the Coulomb potential  $-Ze^2/r_i$  due to the nuclear attraction. As is well known, the difficulties in solving this problem reside in the second term, the Coulomb interaction between the electrons. For heavy atoms, exact solutions require a prohibitive amount of computation, while any possibility of an exact solution for the electronic states in a metal is clearly out of the question. It is therefore necessary to replace the Coulomb interaction by a self-consistent field, which is most satisfactorily determined by means of the density-functional theory of Hohenberg and Kohn (1964) and Kohn and Sham (1965).

The first step is to write the Hamiltonian (1.2.2) in the symbolic form

$$\mathcal{H} = T + U + V, \quad (1.2.3)$$

incorporating the kinetic energy, the Coulomb repulsion between the electrons, and the external potential, due to the nucleus in the atom or

the periodic lattice potential in the solid. Hohenberg and Kohn (1964) established two important results. Firstly, they showed that the external potential is a unique functional of the electron density  $n(\mathbf{r})$ , and hence that the ground-state wavefunction  $\Phi$  and the energy functional

$$\langle \Phi | \mathcal{H} | \Phi \rangle = \langle \Phi | (T + U) | \Phi \rangle + \int v_{\text{ext}}(\mathbf{r})n(\mathbf{r})d\mathbf{r} \quad (1.2.4)$$

are unique functionals of  $n(\mathbf{r})$ . Secondly, they proved that the energy functional (1.2.4) attains its minimum value, the ground-state energy, for the correct ground-state density. Hence, if the universal functional  $\langle \Phi | (T + U) | \Phi \rangle$  were known, it would be straightforward to use this variational principle to determine the ground-state energy for any specified external potential. However, the functional is not known, and the complexity of the many-electron problem is associated with its approximate determination.

Guided by the successes of the one-electron model, Kohn and Sham (1965) considered a system of non-interacting electrons with the same density as that of the real system, satisfying the single-particle Schrödinger equation

$$\left[ -\frac{\hbar^2}{2m}\nabla^2 + v_{\text{eff}}(\mathbf{r}) \right] \psi_i(\mathbf{r}) = \varepsilon_i \psi_i(\mathbf{r}). \quad (1.2.5)$$

The ground state  $\Phi_S$  of such a system is just the antisymmetrized product, or *Slater determinant*, formed from the  $Z$  lowest-lying one-electron orbitals, so that the electron density is the sum over these orbitals:

$$n(\mathbf{r}) = \sum_i^Z |\psi_i(\mathbf{r})|^2. \quad (1.2.6)$$

The effective potential  $v_{\text{eff}}(\mathbf{r})$  must therefore be determined so that  $n(\mathbf{r})$  is also the ground-state density of the real system. To accomplish this, the energy functional (1.2.4) may be written in the form

$$\begin{aligned} \langle \Phi | \mathcal{H} | \Phi \rangle &= \langle \Phi_S | T | \Phi_S \rangle \\ &+ \int \left[ \frac{1}{2} \int \frac{e^2 n(\mathbf{r}')}{|\mathbf{r} - \mathbf{r}'|} d\mathbf{r}' + v_{\text{ext}}(\mathbf{r}) \right] n(\mathbf{r}) d\mathbf{r} + E_{\text{xc}}\{n(\mathbf{r})\}, \end{aligned} \quad (1.2.7)$$

where the first contribution is the kinetic energy of the non-interacting system, and the second is the Hartree energy of the charge cloud. The last term is the difference between the true kinetic energy and that of the non-interacting system, plus the difference between the true interaction energy of the system and the Hartree energy. This exchange-correlation

energy encompasses our ignorance of this problem, and is presumably relatively small. In the *local* approximation, which is adopted to convert the density-functional theory into a practical method, this energy is written

$$E_{\text{xc}}\{n(\mathbf{r})\} \approx \int \varepsilon_{\text{xc}}[n(\mathbf{r})]n(\mathbf{r})d\mathbf{r}, \quad (1.2.8)$$

and the effective potential is therefore

$$v_{\text{eff}}(\mathbf{r}) = \int \frac{e^2 n(\mathbf{r}')}{|\mathbf{r} - \mathbf{r}'|} d\mathbf{r}' + v_{\text{ext}}(\mathbf{r}) + v_{\text{xc}}[n(\mathbf{r})], \quad (1.2.9)$$

where

$$v_{\text{xc}}[n(\mathbf{r})] = d[n\varepsilon_{\text{xc}}(n)]/dn \equiv \mu_{\text{xc}}[n(\mathbf{r})] \quad (1.2.10)$$

is the local approximation to the exchange-correlation contribution to the chemical potential of the electron gas. Useful estimates of this quantity have been obtained from calculations for a homogeneous electron gas of density  $n(\mathbf{r})$  by Hedin and Lundqvist (1971), von Barth and Hedin (1972), and Gunnarsson and Lundqvist (1976), and these are frequently used in calculations on both atoms and solids.

In order to determine the atomic structure, the Schrödinger equation (1.2.5) must be solved by the Hartree self-consistent procedure, in which, through a process of iteration, the potential (1.2.9) generates wavefunctions which, via (1.2.6), reproduce itself. Since this potential is spherically symmetric in atoms, the single-particle wavefunctions may be written as the product of a radial function, a spherical harmonic and a spin function

$$\psi_{nlm_l m_s}(\mathbf{r}\sigma) = i^l R_{nl}(r) Y_{lm_l}(\hat{\mathbf{r}}) \chi_{m_s}, \quad (1.2.11)$$

where  $\hat{\mathbf{r}}$  is a unit vector in the direction of  $\mathbf{r}$ , the spin quantum number  $m_s$  can take the values  $\pm\frac{1}{2}$ , and the phase factor  $i^l$  is included for later convenience. The radial component satisfies the equation

$$-\frac{\hbar^2}{2m} \frac{d^2[rR_{nl}(r)]}{dr^2} + \left( v_{\text{eff}}(r) + \frac{l(l+1)\hbar^2}{2mr^2} - \varepsilon \right) [rR_{nl}(r)] = 0. \quad (1.2.12)$$

Some radial wavefunctions for rare earth atoms are shown in Fig. 1.1. The  $4f$  electrons are well embedded within the atom, and shielded by the  $5s$  and  $5p$  states from the surroundings. The  $5d$  and  $6s$  electrons form the conduction bands in the metals. The incomplete screening of the increasing nuclear charge along the rare earth series causes the lanthanide contraction of the wavefunctions, which is reflected in the ionic and atomic radii in the solid state. In particular, as illustrated in Fig. 1.1, the  $4f$  wavefunction contracts significantly between Ce, which has

one  $4f$  electron, and Tm, which has one  $4f$  hole in the atom, though two in the metallic state. The angular dependences of the  $4f$  wavefunctions are depicted in Fig. 1.2. The charge clouds are highly anisotropic, with pronounced multipoles whose magnitudes and signs change dramatically with  $m_l$ . As we shall see, this anisotropy is clearly manifested in the magnetic properties of the metals.

Since they are among the heavier elements, relativistic effects are of substantial importance in the rare earths. These are most straightforwardly taken into account by solving the Dirac equation in the central

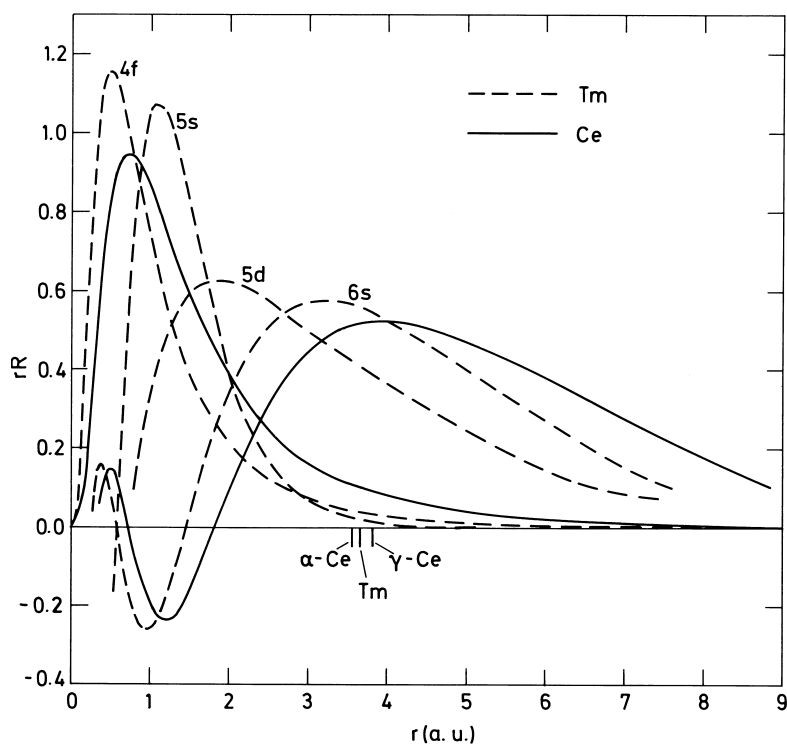


**Fig. 1.1.** The radial components of atomic wavefunctions for Ce, which has one  $4f$  electron, and Tm, which has 13  $4f$  electrons, or one  $4f$  hole. The Tm wavefunctions are contracted, relative to those of Ce, due to the incomplete shielding of the greater nuclear charge. As a consequence, the amplitude of the  $4f$  wavefunction at the indicated Wigner–Seitz radius is much greater in Ce than in Tm, which has important consequences for the character of the  $4f$  states in the metals.

field, rather than the Schrödinger equation, but it may be more instructive to consider them as perturbations which, to order  $(p/mc)^2$ , augment the one-electron potential with

$$-\frac{p^4}{8m^3c^2} - \frac{\hbar^2}{4m^2c^2} \frac{dv}{dr} \frac{\partial}{\partial r} + \frac{1}{2m^2c^2r} \frac{dv}{dr} \mathbf{s} \cdot \mathbf{l}. \quad (1.2.13)$$

The first term, which is due to the increase of mass with velocity, reduces the energy of all states by an amount which decreases with  $l$ , while the second ‘Darwin’ term increases the energy of  $s$  states only. These effects may both be incorporated into the central field, but the last term couples together the spin and orbital motion in a way that has far-reaching consequences for the magnetic properties.

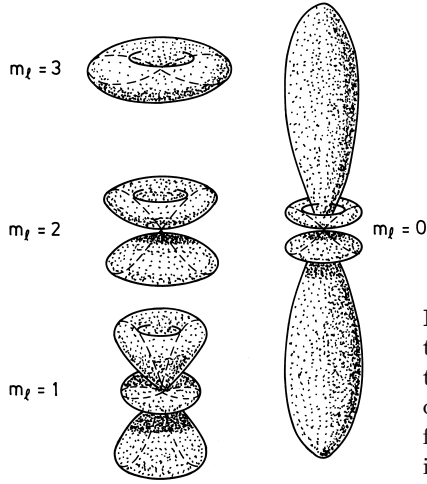


**Fig. 1.2.** The angular variation of the  $4f$  wavefunctions. The interaction of the highly anisotropic charge clouds with the crystalline electric fields gives rise to the large single-ion anisotropies observed in the rare earth metals.

In the Russell–Saunders coupling scheme, which is an accurate procedure for the  $4f$  electrons, the spins  $\mathbf{s}_i$  of the individual  $4f$  electrons are coupled by the exchange interaction, diagonal in the total spin  $\mathbf{S}$  of the incompletely filled subshell, while the Coulomb interaction similarly combines the  $\mathbf{l}_i$  into the total orbital momentum  $\mathbf{L}$ . In terms of the one-electron functions, the wavefunction for the subshell may be written

$$\Psi(LSM_LM_S) = \sum_{m_l m_s} C(LSM_LM_S; m_l m_s) \psi(m_l m_s), \quad (1.2.14)$$

where the  $C(LSM_LM_S; m_l m_s)$  are the *Clebsch–Gordan* or *Wigner* coefficients. It is convenient to write this expansion in a representation-

independent form, in terms of the state vectors

$$|LSM_L M_S\rangle = \sum_{m_l m_s} \langle m_l m_s | LSM_L M_S \rangle |m_l m_s\rangle. \quad (1.2.15)$$

The exchange and Coulomb interactions are sufficiently large that the magnetic properties at all accessible temperatures are determined by the  $S$  and  $L$  states of lowest energy. These are found from Hund's rules;  $S$  is maximized and, subject to this maximum  $S$  value,  $L$  is also maximized. This results in the values for the trivalent ions shown in Table 1.1.

**Table 1.1.** Properties of the tripositive rare earth ions.

$4f^n$	Ion <sup>+++</sup>	$L$	$S$	$J$	$g$	$(g-1)^2 J(J+1)$	$\Delta(K)$
0	La	0	0	0	—		
1	Ce	3	$\frac{1}{2}$	$\frac{5}{2}$	$\frac{6}{7}$	0.18	3150
2	Pr	5	1	4	$\frac{4}{5}$	0.80	3100
3	Nd	6	$\frac{3}{2}$	$\frac{9}{2}$	$\frac{8}{11}$	1.84	2750
4	Pm	6	2	4	$\frac{3}{5}$	3.20	2300
5	Sm	5	$\frac{5}{2}$	$\frac{5}{2}$	$\frac{2}{7}$	4.46	1450
6	Eu	3	3	0	—		500
7	Gd	0	$\frac{7}{2}$	$\frac{7}{2}$	2	15.75	
8	Tb	3	3	6	$\frac{3}{2}$	10.50	2900
9	Dy	5	$\frac{5}{2}$	$\frac{15}{2}$	$\frac{4}{3}$	7.08	4750
10	Ho	6	2	8	$\frac{5}{4}$	4.50	7500
11	Er	6	$\frac{3}{2}$	$\frac{15}{2}$	$\frac{6}{5}$	2.55	9350
12	Tm	5	1	6	$\frac{7}{6}$	1.17	11950 <sup>a</sup>
13	Yb	3	$\frac{1}{2}$	$\frac{7}{2}$	$\frac{8}{7}$	0.32	14800
14	Lu	0	0	0	—		

<sup>a</sup> The lowest excited state in Tm is  $^3F_4$  at 8490K.

It is a consequence of the *Wigner-Eckart theorem* that the spin-orbit term in (1.2.13) can be written

$$\mathcal{H}_{\text{so}} = \pm \zeta(LS) \mathbf{S} \cdot \mathbf{L}, \quad (1.2.16)$$

where

$$\zeta(LS) = \frac{\pi}{m^2 c^2 S} \int r R_{4f}^2(r) \frac{dv}{dr} dr, \quad (1.2.17)$$

and the + and – signs refer respectively to a less or more than half-filled subshell. The spin and orbital angular momenta are thus combined into the total angular momentum  $\mathbf{J} = \mathbf{L} + \mathbf{S}$ . These states may be written

$$|JM_JLS\rangle = \sum_{M_L M_S} \langle LSM_L M_S | JM_JLS\rangle |LSM_L M_S\rangle. \quad (1.2.18)$$

Because of the sign of (1.2.16), the value of  $J$  in the ground state is  $L \mp S$ , according as the subshell is less or more than half-full. Roughly speaking,  $\mathbf{L}$  is always parallel to  $\mathbf{J}$ , but  $\mathbf{S}$  is antiparallel in the first half of the series and parallel in the second half. The energy separation to the first excited multiplet may be determined from the matrix elements of (1.2.16), and is given by

$$\Delta = \zeta(LS) \begin{cases} (J+1) \\ J \end{cases} \quad (1.2.19)$$

again depending on whether the subshell is respectively less or more than half-filled. The values of  $J$  in the ground state and of  $\Delta$ , obtained from spectroscopic measurements on rare earth salts (Dieke 1968), are given in Table 1.1.

The magnetization of an assembly of  $N$  rare earth atoms or ions is given by the derivative of the free energy with respect to magnetic field:

$$M = -\frac{1}{V} \frac{\partial F}{\partial H} \quad (1.2.20)$$

or, recalling that

$$F = -\frac{N}{\beta} \ln \sum_n e^{-\beta E_n(H)}, \quad (1.2.21)$$

where  $E_n(H)$  are the atomic energy levels in the field, and  $\beta = 1/k_B T$ ,

$$M = \frac{N}{V} \sum_n -\frac{\partial E_n}{\partial H} e^{-\beta E_n} / \sum_n e^{-\beta E_n}. \quad (1.2.22)$$

Neglecting the small diamagnetic susceptibility, the magnetic contribution to the Hamiltonian is given by the Zeeman term

$$\mathcal{H}_Z = -\mu_B (\mathbf{L} + g_0 \mathbf{S}) \cdot \mathbf{H}, \quad (1.2.23)$$

where  $\mu_B$  is the Bohr magneton. Because of the negative charge on the electron, the angular momentum and the magnetic moment are *antiparallel*. This gives rise to certain difficulties, which are frequently ignored in the literature. We shall circumvent them by taking  $\mathbf{L}$ ,  $\mathbf{S}$ , and  $\mathbf{J}$  as

signifying the *negative* of the corresponding angular-momentum vector. We shall furthermore from now on take the gyromagnetic ratio  $g_0$  as 2. Second-order perturbation theory then gives the magnetic contribution to the energy:

$$\delta E_n(H) = -\mu_B \mathbf{H} \cdot \langle n | \mathbf{L} + 2\mathbf{S} | n \rangle + \sum_{m \neq n} \frac{|\langle n | \mu_B \mathbf{H} \cdot (\mathbf{L} + 2\mathbf{S}) | m \rangle|^2}{E_n - E_m}. \quad (1.2.24)$$

Problems of degeneracy are taken care of by using the  $|JM_JLS\rangle$  basis, whose degeneracy is completely lifted by the field. In this basis, and within a particular  $JLS$ -multiplet, the Wigner-Eckart theorem implies that the matrix elements of  $(\mathbf{L} + 2\mathbf{S})$  are proportional to those of  $\mathbf{J}$ , so that

$$\langle JLSM_J | \mathbf{L} + 2\mathbf{S} | JLSM'_J \rangle = g(JLS) \langle JLSM_J | \mathbf{J} | JLSM'_J \rangle, \quad (1.2.25)$$

and the proportionality constant, *the Landé factor*, is

$$g = \frac{3}{2} + \frac{S(S+1) - L(L+1)}{2J(J+1)}. \quad (1.2.26)$$

Within this multiplet, we may write eqn (1.2.25) in the shorthand form  $\mathbf{L} + 2\mathbf{S} = g\mathbf{J}$ , and consider the effective moment on the atom to be

$$\boldsymbol{\mu} = g\mu_B \mathbf{J}. \quad (1.2.27)$$

With the same proviso, we may similarly write

$$\mathbf{L} = (2 - g)\mathbf{J}, \quad (1.2.28)$$

and

$$\mathbf{S} = (g - 1)\mathbf{J}. \quad (1.2.29)$$

If  $J$  is non-zero, the first-order term in (1.2.24), combined with (1.2.22) gives a magnetization for the ground-state multiplet:

$$M(H, T) = \frac{N}{V} g\mu_B J B_J(\beta g\mu_B JH), \quad (1.2.30)$$

where the *Brillouin function* is

$$B_J(x) = \frac{2J+1}{2J} \coth \frac{2J+1}{2J} x - \frac{1}{2J} \coth \frac{1}{2J} x. \quad (1.2.31)$$

If  $g\mu_B JH$  is small compared with  $k_B T$ , the susceptibility is constant and given by *Curie's law*:

$$\chi = \frac{M}{H} = \frac{g^2 \mu_B^2 J(J+1) N}{3k_B T} \frac{1}{V} \equiv \frac{C}{T}, \quad (1.2.32)$$

where  $C$  is the *Curie constant*. The second-order non-diagonal term in (1.2.24) gives a paramagnetic contribution to  $\chi$  which is independent of temperature, provided that the thermal population of the excited states is negligible. This *Van Vleck paramagnetism* is very small in the heavy rare earths, but in the first half of the series it is given by

$$\chi_V = \frac{2\mu_B^2(L+1)S}{3(J+1)\Delta} \frac{N}{V}, \quad (1.2.33)$$

which may be significant, since

$$\frac{\chi_V}{\chi} = \frac{2(L+1)S}{g^2J(J+1)^2} \frac{k_B T}{\Delta} = \frac{\alpha k_B T}{\Delta}, \quad (1.2.34)$$

where, from Table 1.1,  $\alpha$  takes the modest value of 0.19 for Pr, but is 12 for Sm. Since  $\Delta$  is only 1450 K, the Van Vleck paramagnetism in Sm is significant even at rather low temperatures. In trivalent Eu,  $J = 0$  in the ground state and the paramagnetic susceptibility is due entirely to the mixing of the excited states into the ground state by the field, and to the thermal excitation of these states. However, Eu metal is divalent and the  $^8S_{7/2}$  ionic susceptibility follows Curie's law very closely. The Van Vleck paramagnetism arising from the mixing of states of different  $J$  will not play a significant role in our later discussion, but the analogous phenomenon of the mixing of states of different  $M_J$ , split by the crystalline electric field in the metal, will be of central importance.

### 1.3 The metallic state

When a large number of rare earth atoms are assembled to form a solid, the  $4f$  electrons generally remain localized, in a sense which will be made more precise later, so that their magnetic properties closely resemble those in the free atoms. The external  $5d$  and  $6s$  electrons, on the other hand, become delocalized into *Bloch states*, extending throughout the metal and constituting the conduction-electron gas. The conduction electrons themselves make only a modest contribution to the magnetic moment, but by mediating the magnetic interactions they play a crucial role in determining the characteristic magnetic properties in the solid state. An understanding of the magnetism therefore requires a detailed description of the conduction electron gas, and this section is concerned with our theoretical and experimental knowledge of the Bloch states, and their influence on the structural properties of the metals. Some of these structural properties of the rare earth metals are collected in Table 1.2, from which it may be seen that the room-temperature structures are all close-packed, with a coordination number of 12, with the exception of Eu, which is bcc. The remaining elements all form hexagonal phases,

**Table 1.2.** Structural properties of the lanthanides.

Element	Structure (300 K)	Lattice const.		Atomic rad. $S$ (a.u.)	Density (g/cm <sup>3</sup> )	Melt. point (K)
		$a$ (Å)	$c$ (Å)			
La	dhcp	3.774	12.171	3.92	6.146	1191
Ce( $\beta$ )	dhcp	3.681	11.857	3.83	6.689	1071
Ce( $\gamma$ )	fcc	5.161		3.81	6.770	
Ce( $\alpha$ )	fcc	4.85 (77 K)		3.58	8.16	
Pr	dhcp	3.672	11.833	3.82	6.773	1204
Nd	dhcp	3.658	11.797	3.80	7.008	1294
Pm	dhcp	3.65	11.65	3.78	7.264	1315
Sm	rhomb	3.629	26.207	3.77	7.520	1347
Eu	bcc	4.583		4.26	5.244	1095
Gd	hcp	3.634	5.781	3.76	7.901	1586
Tb	hcp	3.606	5.697	3.72	8.230	1629
Dy	hcp	3.592	5.650	3.70	8.551	1687
Ho	hcp	3.578	5.618	3.69	8.795	1747
Er	hcp	3.559	5.585	3.67	9.066	1802
Tm	hcp	3.538	5.554	3.65	9.321	1818
Yb	fcc	5.485		4.05	6.966	1092
Lu	hcp	3.505	5.549	3.62	9.841	1936

although the hcp allotrope of Yb is only stable at low temperatures, and Ce has two separate fcc phases in addition to its dhcp form.

The heavy rare earths are all hcp, while the dhcp structure predominates among the lighter metals. These structures may be produced by stacking close-packed layers in the sequences ABAB and ABAC respectively, as shown in Fig. 1.3. The fcc structure corresponds to the stacking sequence ABCABC, while the Sm structure is ABABCBCAC. The latter has rhombohedral symmetry but it is frequently more convenient to consider it as hexagonal. The crystallographic  $a$ -axis is taken along the direction joining a pair of nearest neighbours in the hexagonal plane, the  $c$ -axis is normal to the plane, and the  $b$ -axis is orthogonal to the other two. The local, i.e. nearest-neighbour, symmetry in the fcc and hcp structure is, of course, cubic and hexagonal respectively. The dhcp structure, on the other hand, has two types of site and, for an ‘ideal’  $c/2a$  ratio of 1.633, their *local* symmetry alternates between cubic and hexagonal in the sequence chch, while the Sm structure corresponds to chhchh. As may be seen from Table 1.2, however, the  $c/2a$  ratio is consistently smaller than the ideal value, so the ‘cubic’ sites have only approximate local cubic symmetry.

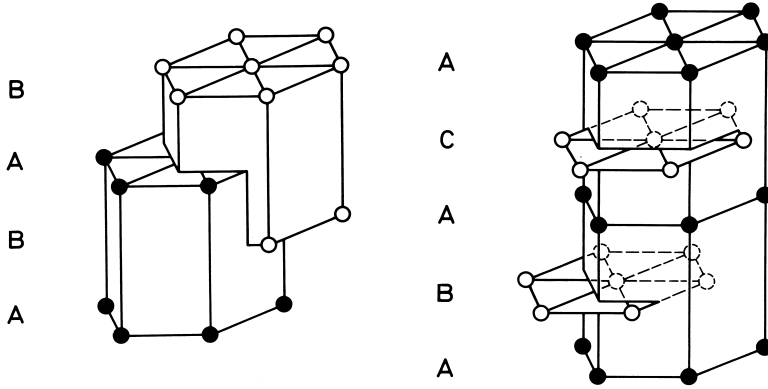


**Fig. 1.3.** The hcp and dhcp crystal structures. In the latter, the B and C sites have hexagonal symmetry, while the A sites have local cubic symmetry, for an ideal  $c/a$  ratio.

To determine the eigenstates for the conduction electron gas, we adopt the same procedure as that outlined for atoms in the previous section. The external potential  $v_{\text{ext}}(\mathbf{r})$  in (1.2.2) is now the Coulomb attraction of the nuclei situated on the crystal lattice, shielded by the electrons of the ionic core, which are usually taken to have the same charge distribution as in the atoms. The potential consequently has the translational symmetry of the periodic lattice, and so therefore does the effective potential  $v_{\text{eff}}(\mathbf{r})$ , which arises when we make the single-particle approximation (1.2.5) and the local-density approximation (1.2.9). In the atom, the eigenfunctions are determined by the boundary condition that their amplitude must vanish for large values of  $r$  and, when (1.2.12) is integrated numerically, they are automatically continuous and differentiable. The translational symmetry of the solid is expressed in *Bloch's theorem*:

$$\psi(\mathbf{r}) = e^{i\mathbf{k}\cdot\mathbf{R}} \psi(\mathbf{r} - \mathbf{R}), \quad (1.3.1)$$

and this boundary condition gives rise to eigenfunctions  $\psi_j(\mathbf{k}, \varepsilon, \mathbf{r})$  and eigenvalues  $\varepsilon_j(\mathbf{k})$  which are functions of the wave-vector  $\mathbf{k}$  in reciprocal space. All the electron states may be characterized by values of  $\mathbf{k}$  lying within the *Brillouin zone*, illustrated for the hexagonal and fcc structures in Fig. 1.4, and by the band index  $j$  defined such that  $\varepsilon_j(\mathbf{k}) \leq \varepsilon_{j+1}(\mathbf{k})$ .

The determination of the eigenstates of the Schrödinger equation, subject to the Bloch condition (1.3.1) is the central problem of energy-band theory. It may be solved in a variety of ways, but by far the most

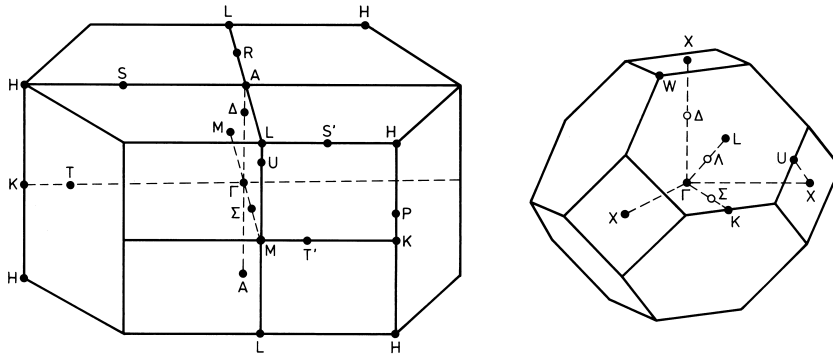


**Fig. 1.4.** The Brillouin zones for the hexagonal and fcc lattices.

effective procedure for the rare earths is to adopt one of the linear methods of Andersen (1975). In the following, we will use the *Atomic Sphere Approximation* (ASA) which will allow us to illustrate the construction and characteristics of the energy bands in a transparent way. This approximation, and the closely-related *Linear Muffin-Tin Orbitals Method* (LMTO), which allows computationally very efficient calculations of arbitrarily precise energy bands, for a given potential, have been concisely described by Mackintosh and Andersen (1980) and, in much more detail, by Skriver (1984).

In a close-packed solid, the electrons may to a very good approximation be assumed to move in a *muffin-tin potential*, which is spherically symmetric in a sphere surrounding each atomic site, and constant in the interstitial regions. We recall that the *atomic polyhedron*, or *Wigner-Seitz cell*, is bounded by the planes which perpendicularly bisect the vectors joining an atom at the origin with its neighbours, and has the same volume as the *atomic sphere*, whose radius  $S$  is chosen accordingly. If we surround each site in the crystal with an atomic sphere, the potential within each of these overlapping regions will, to a high degree of accuracy, be spherically symmetric. Neglecting the spin, we may therefore write the solutions of the Schrödinger equation for a single atomic sphere situated at the origin in the form

$$\psi_{lm}(\varepsilon, \mathbf{r}) = i^l R_l(\varepsilon, r) Y_{lm}(\hat{\mathbf{r}}), \quad (1.3.2)$$

where the radial function  $R_l(\varepsilon, r)$  satisfies eqn (1.2.12) and is a function of the continuous energy variable  $\varepsilon$ . Examples of such radial functions are shown in Fig. 1.5.

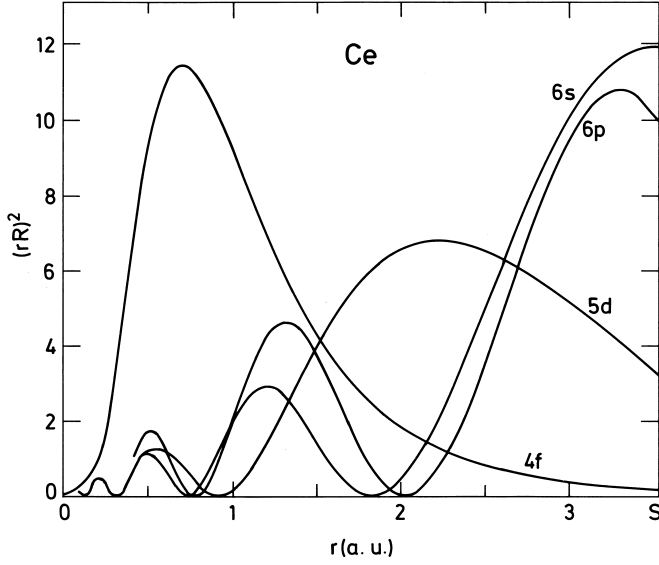


**Fig. 1.5.** Radial wavefunctions for  $\alpha$ -Ce metal, calculated by Skriver from the self-consistent atomic-sphere potential, at the energies  $C_{nl}$  of the centres of the associated bands. Since these wavefunctions are normalized within the unit cell, the effective masses  $\mu_{nl}$  are inversely proportional to the value of  $R_l^2(C_{nl}, S)$  at the Wigner-Seitz radius, and this probability, and the consequent overlap between wavefunctions on neighbouring sites, therefore determines the corresponding band width.

Augmenting these partial waves by suitably-chosen regular solutions of Laplace's equation, we define the energy-dependent *muffin-tin orbitals*

$$\chi_{lm}(\varepsilon, \mathbf{r}) = i^l Y_{lm}(\hat{\mathbf{r}}) \begin{cases} R_l(\varepsilon, r) + p_l(\varepsilon)(r/S)^l; & r < S \\ (S/r)^{l+1} & ; \quad r > S, \end{cases} \quad (1.3.3)$$

which are continuous and differentiable if

$$p_l(\varepsilon) = \frac{D_l(\varepsilon) + l + 1}{D_l(\varepsilon) - l}, \quad (1.3.4)$$

where the *logarithmic derivative* is

$$D_l(\varepsilon) = S \frac{R_l'(\varepsilon, S)}{R_l(\varepsilon, S)}. \quad (1.3.5)$$

From muffin-tin orbitals located on the lattice sites of a solid, with one atom per unit cell, we now construct a wavefunction which is continuous and differentiable, and manifestly satisfies the Bloch condition (1.3.1):

$$\psi_j(\mathbf{k}, \varepsilon, \mathbf{r}) = \sum_{lm} a_{lm}^{jk} \sum_{\mathbf{R}} e^{i\mathbf{k}\cdot\mathbf{R}} \chi_{lm}(\varepsilon, \mathbf{r} - \mathbf{R}). \quad (1.3.6)$$

If we approximate the atomic polyhedra by spheres, and implicitly assume that they fill space, the condition that (1.3.6) is a solution of the Schrödinger equation is easily seen to be that the sum of the tails originating from terms of the form  $(S/|\mathbf{r} - \mathbf{R}|)^{l+1}$ , from the surrounding atoms, cancels the 'extra' contribution

$$\sum_{lm} a_{lm}^{jk} Y_{lm}(\hat{\mathbf{r}}) p_l(\varepsilon) (r/S)^l,$$

in the atomic sphere at the origin. To satisfy this condition, we expand the tails of the muffin-tin orbitals centred at  $\mathbf{R}$  about the origin, in the form

$$\begin{aligned} \sum_{\mathbf{R} \neq \mathbf{0}} e^{i\mathbf{k}\cdot\mathbf{R}} \left( \frac{S}{|\mathbf{r} - \mathbf{R}|} \right)^{l+1} i^l Y_{lm}(\widehat{\mathbf{r} - \mathbf{R}}) \\ = \sum_{l'm'} \frac{-1}{2(2l'+1)} \left( \frac{r}{S} \right)^{l'} i^{l'} Y_{l'm'}(\hat{\mathbf{r}}) \mathcal{S}_{l'm',lm}^{\mathbf{k}}, \end{aligned} \quad (1.3.7)$$

where the expansion coefficients, known as the *canonical structure constants*, are

$$\mathcal{S}_{l'm',lm}^{\mathbf{k}} = \sum_{\mathbf{R} \neq \mathbf{0}} e^{i\mathbf{k}\cdot\mathbf{R}} \mathcal{S}_{l'm',lm}(\mathbf{R}), \quad (1.3.8)$$

with

$$\mathcal{S}_{l'm',lm}(\mathbf{R}) = g_{l'm',lm} \sqrt{4\pi} (-i)^\lambda Y_{\lambda\mu}^*(\hat{\mathbf{R}}) (R/S)^{-\lambda-1},$$

where

$$g_{l'm',lm} \equiv (-1)^{m+1} 2 \sqrt{\frac{(2l'+1)(2l+1)}{2\lambda+1} \frac{(\lambda+\mu)!(\lambda-\mu)!}{(l'+m')!(l'-m')!(l+m)!(l-m)!}}$$

and

$$\lambda \equiv l + l' \quad ; \quad \mu \equiv m - m'.$$

From (1.3.3) and (1.3.7), the required *tail-cancellation* occurs if

$$\sum_{lm} [P_l(\varepsilon) \delta_{l'l} \delta_{m'm} - \mathcal{S}_{l'm',lm}^{\mathbf{k}}] a_{lm}^{jk} = 0, \quad (1.3.9)$$

where the *potential function*  $P_l(\varepsilon)$  is defined by

$$P_l(\varepsilon) = 2(2l + 1)p_l(\varepsilon) = 2(2l + 1) \frac{D_l(\varepsilon) + l + 1}{D_l(\varepsilon) - l}. \quad (1.3.10)$$

The linear homogeneous equations (1.3.10) have solutions for the eigenvectors  $a_{lm}^{jk}$  only for those values of  $\mathbf{k}$  and  $\varepsilon$  for which

$$\det[P_l(\varepsilon)\delta_{l'l}\delta_{m'm} - \mathcal{S}_{l'm',lm}^{\mathbf{k}}] = 0. \quad (1.3.11)$$

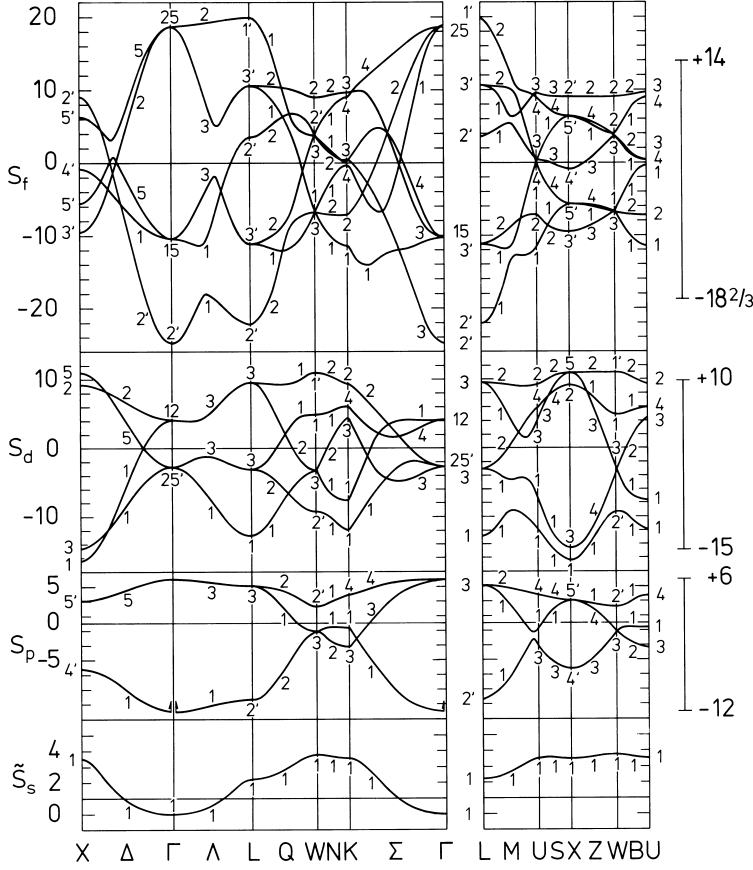


**Fig. 1.6.** The canonical bands for the fcc structure. The band structure in the metal may be obtained by placing, scaling, and distorting the canonical bands according to the values of the corresponding potential parameters  $C_{nl}$ ,  $\mu_{nl}$ , and  $\gamma_{nl}$ , and finally hybridizing them. The extent of the bands, according to the Wigner-Seitz rule, is indicated on the right.

In this determinantal equation for the band structure  $\varepsilon_j(\mathbf{k})$ , the information about the structure is separated from that on the potential. The structure constants  $\mathcal{S}_{l'm',lm}^{\mathbf{k}}$  are canonical in the sense that they depend only on the crystal structure and not, for example, on the lattice constant, as may be seen from the definition (1.3.8), and the potential function  $P_l(\varepsilon)$  is determined entirely by the potential within the atomic sphere. We shall consider these two terms in turn.

If we include values of  $l$  up to 3, i.e.  $s, p, d$ , and  $f$  partial waves, the structure constants form a square matrix with 16 rows and columns. The terms with  $l = l'$  fall into 4 blocks, and these submatrices may be diagonalized by a unitary transformation from the  $lm$  to an  $lj$  representation. The  $(2l+1)$  diagonal elements  $\mathcal{S}_{lj}^{\mathbf{k}}$  of each sub-block are the unhybridized *canonical  $l$  bands*. The canonical bands for the fcc structure are shown in Fig. 1.6. If hybridization is neglected, which corresponds to setting to zero the elements of  $\mathcal{S}_{l'm',lm}^{\mathbf{k}}$  with  $l \neq l'$ , eqn (1.3.11) takes the simple form

$$P_l(\varepsilon) = \mathcal{S}_{lj}^{\mathbf{k}}. \quad (1.3.12)$$

Since  $P_l(\varepsilon)$  is a monotonically increasing function of energy, as illustrated in Fig. 1.7, the band energies  $\varepsilon_{lj}(\mathbf{k})$  for the pure  $l$  bands are obtained by a monotonic scaling of the corresponding canonical bands.  $P_l(\varepsilon)$  does not, furthermore, depart greatly from a straight line in the energy region over which a band is formed, so the canonical bands resemble the energy bands in the solid quite closely, whence the name.

The potential function  $P_l(\varepsilon)$  and the logarithmic-derivative function  $D_l(\varepsilon)$  are related to each other through the definition (1.3.10), and this relationship is shown schematically in Fig. 1.7. It is convenient and illuminating to parametrize the potential function, when considering the formation of the energy bands from the canonical bands. The poles of  $P_l(\varepsilon)$ , which occur when  $D_l(\varepsilon) = l$ , divide the energy into regions in which lie the corresponding atomic energy-levels  $\varepsilon_{nl}$ . The energies  $V_{nl}$  which separate these regions are defined by

$$D_l(V_{nl}) = l \quad (1.3.13)$$

and, within a particular region, the energy  $C_{nl}$  of the centre of the band is fixed by the condition that  $P_l(C_{nl}) = 0$ , or

$$D_l(C_{nl}) = -(l+1). \quad (1.3.14)$$

The allowed  $\mathbf{k}$ -values corresponding to this energy are just those for

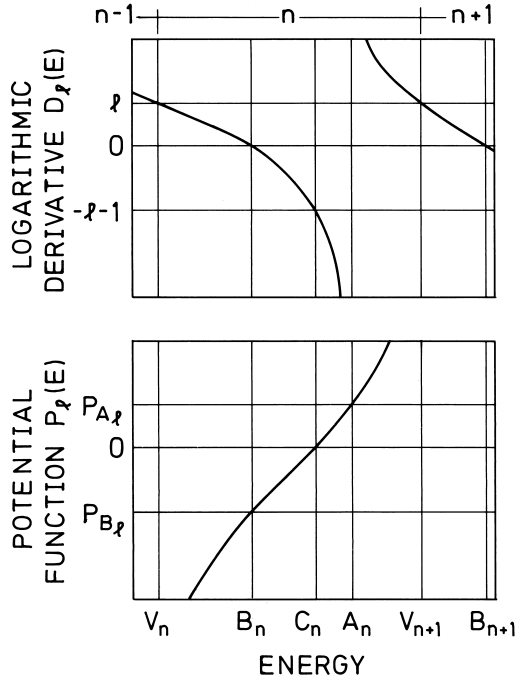


**Fig. 1.7.** The  $n$ th period of the logarithmic derivative function  $D_l(\varepsilon)$ , and the corresponding potential function  $P_l(\varepsilon)$ . The bottom, centre, and top of the  $nl$  band are defined respectively by  $P_l(B_{nl}) = -2(2l+1)(l+1)/l$  ( $D_l(B_{nl}) = 0$ ),  $P_l(C_{nl}) = 0$ , and  $P_l(A_{nl}) = l$  ( $D_l(A_{nl}) = -\infty$ ).

which  $S_{lj}^k = 0$  and, since the average over the Brillouin zone may be shown to vanish, i.e.

$$\sum_{j=1}^{2l+1} \int_{BZ} S_{lj}^k d\mathbf{k} = 0, \quad (1.3.15)$$

the designation of  $C_{nl}$  as the centre of the band is appropriate. Equation (1.3.12) may be satisfied, and energy bands thereby formed, over an energy range around  $C_{nl}$  which, to a good approximation, is defined by the Wigner–Seitz rule, which states that, by analogy with molecular binding, the top and bottom of the band occur where the radial wavefunction and its derivative respectively are zero on the atomic sphere. The corresponding energies, defined by

$$D_l(A_{nl}) = -\infty \quad (1.3.16)$$

and

$$D_l(B_{nl}) = 0, \quad (1.3.17)$$

are then known respectively as the top and bottom of the  $nl$  band, even though this designation is not precisely accurate.

Over the energy range  $A_{nl}-B_{nl}$ , the potential function may be parametrized with reasonable accuracy as

$$P_l(\varepsilon) \simeq \frac{1}{\gamma_{nl}} \frac{\varepsilon - C_{nl}}{\varepsilon - V_{nl}}. \quad (1.3.18)$$

It is convenient to define the related mass parameter  $\mu_{nl}$  by

$$\mu_{nl} S^2 = \left. \frac{dP_l(\varepsilon)}{d\varepsilon} \right|_{C_{nl}} \simeq \frac{1}{\gamma_{nl}(C_{nl} - V_{nl})}. \quad (1.3.19)$$

It is determined by the probability that an electron described by the partial wave  $R_l(C_{nl}, r)$  reaches the atomic sphere and, if the wavefunction is normalized within the sphere, it may be shown that

$$\mu_{nl} S^2 = \left[ \frac{1}{2} S R_l^2(C_{nl}, S) \right]^{-1}. \quad (1.3.20)$$

For free electrons,  $\mu_{nl} \equiv 1$  for all values of  $n$  and  $l$ .

With this parametrization, we may write down an explicit expression for the unhybridized band energies. From eqns (1.3.12), (1.3.18) and (1.3.19) these are given by

$$\varepsilon_{lj}(\mathbf{k}) = C_{nl} + \frac{1}{\mu_{nl} S^2} \frac{S_{lj}^{\mathbf{k}}}{1 - \gamma_{nl} S_{lj}^{\mathbf{k}}}. \quad (1.3.21)$$

The pure  $l$  bands are thus obtained from the corresponding canonical bands by fixing the position with  $C_{nl}$ , scaling the bandwidth by  $\mu_{nl} S^2$ , and distorting them with  $\gamma_{nl}$ .

Hybridization between bands of different  $l$  is taken into account by including the structure constants with  $l \neq l'$  in (1.3.11), causing a repulsion between energy levels with the same  $\mathbf{k}$  and symmetry, as specified by the labels in Fig. 1.6. Bands of the same symmetry are thus not allowed to cross, and *strong hybridization* instead creates an energy gap. In addition, *weak hybridization* gives rise to a mixing and repulsion between bands which do not cross in the absence of hybridization. In order to complete the calculation of the band structure, the inaccuracies due to approximating the atomic polyhedron by a sphere, and to neglecting higher partial waves, may be conveniently treated together by perturbation theory. In practice, the energy bands are not of course calculated step-wise as described above, but all the steps are performed simultaneously on a computer. Nevertheless, the conceptual description of the procedure as a placing, scaling and distortion of the

canonical bands, according to the values of the potential parameters, with a final hybridization between bands of the same symmetry, allows a clear visualization of the way in which the relatively complex band structure is built up from simpler elements, and of the relation between the eigenstates of the atom and those in the solid.

**Table 1.3.** Electronic parameters for  $\alpha$ -Ce.

	$6s$	$6p$	$5d$	$4f$
$A_l$ (Ry)	2.234	2.698	1.198	0.648
$C_l$ (Ry)	0.620	1.452	0.792	0.628
$B_l$ (Ry)	0.330	0.909	0.409	0.587
$\mu_l$	0.61	0.70	2.18	45.36
$n_l$	0.509	0.245	2.091	1.154
$N_l(\varepsilon_F)$ (Ry $^{-1}$ )	1.81	1.50	6.48	21.11
$\mathcal{P}_l\Omega$ (Ry)	0.195	0.152	-0.219	-0.163

This procedure may be illustrated by considering the construction of the band structure of  $\alpha$ -Ce from its component parts. Partial waves in the atomic sphere at the energies of the band-centres, where  $P_l(\varepsilon) = 0$ , are shown in Fig. 1.5, and the corresponding potential parameters are given in Table 1.3. In this section, we express the energies in Rydbergs, following our general principle of using throughout the book those units which are favoured by practitioners of research in the subject currently under discussion. The  $s$  and  $p$  effective masses are somewhat below 1, and the relative positions of the band centres correspond quite closely to those of the free-electron gas. Through the influence of the  $l$ -dependent centrifugal-potential term in (1.2.12), the  $d$  and  $f$  states are in contrast constrained to the inner regions of the atomic sphere, with the consequence that the  $d$  mass is relatively large (though not as large as in a typical transition metal) and the  $f$  mass is extremely large.

The energy bands of Fig. 1.8 were calculated by an iterative procedure, by Skriver (private communication). The electron density  $n(\mathbf{r})$  is first estimated by, for example, overlapping *atomic* charge densities situated on the lattice sites, and from it the periodic potential  $v_{\text{eff}}(\mathbf{r})$  is constructed, using the local-density approximation (1.2.9). The band structure is then determined for this potential and  $n(\mathbf{r})$  recalculated, in analogy with (1.2.6), by summing over occupied states, those beneath the Fermi level. This procedure is repeated until the potential self-consistently reproduces itself, and the energy bands have converged to the desired accuracy. The band structure can be considered as being

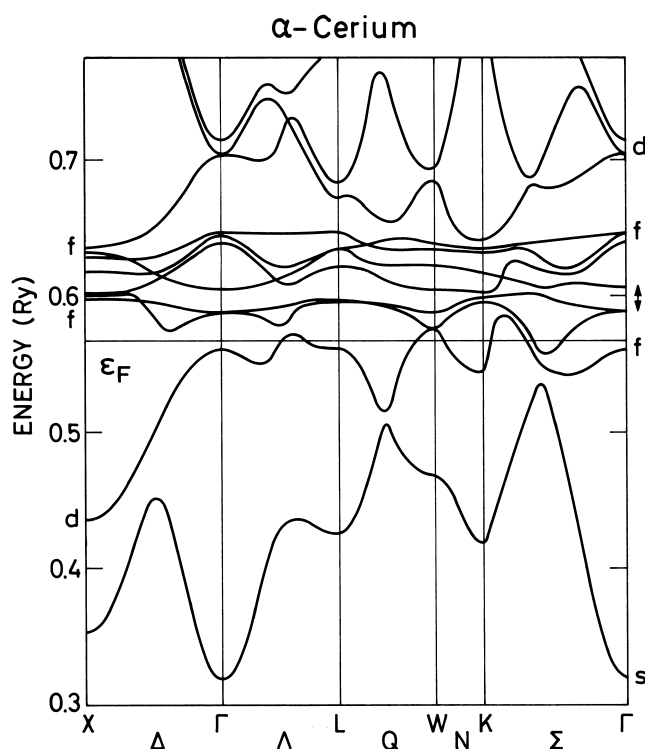


**Fig. 1.8.** The band structure of fcc  $\alpha$ -Ce, calculated by Skriver. The orbital angular momentum of some states at symmetry points in the zone is indicated, including the top and bottom of the narrow bands. The double-headed arrow indicates the spin-orbit splitting of a 4f state.

composed of a broad free-electron-like  $sp$  band, crossed by and hybridizing both strongly and weakly with the  $d$  and  $f$  bands. The occupation numbers  $n_l$  of the various states given in Table 1.3 make it clear that  $\alpha$ -Ce may be classified as both a  $d$ - and an  $f$ -band transition metal.

The above description of the  $f$  states in  $\alpha$ -Ce as occupying the bottom of an  $f$  band is now generally accepted as valid, but the correct treatment of the  $f$  electrons in the rare earth metals, and especially Ce, was a matter of lengthy controversy. According to the standard model, which is generally applicable to rare earth magnetism, an integral number of  $f$  electrons are localized on each ion, subject to the same intra-ionic interactions as in the free atom. The Pauling-Zachariasen promotional model for the  $\gamma$ - $\alpha$  phase transition in Ce, which associated the transition with the transfer of a single  $f$  electron on each ion to a  $d$  state, with a concomitant decrease of about 6% in the fcc lattice

constant, was therefore consistent with the standard model. However the positron-annihilation experiments of Gustafson and Mackintosh (1964) showed that the change in  $f$  occupancy, when the transition was induced by a change in temperature, was much less than one, and indeed that the results in both phases were consistent with about one  $f$  electron per ion. Similar results were obtained by Gustafson *et al.* (1969) when the transition was driven by pressure, and they concluded that it involves not primarily a change in the  $f$  occupancy but rather a change in the  $f$  state, from being localized in the  $\gamma$ -phase to being an itinerant band electron in the  $\alpha$ -phase. This idea was taken up by Johansson (1974) who, from a consideration of spectroscopic, cohesive and thermodynamic evidence, proposed that the  $\gamma$ - $\alpha$  transition should be considered as a Mott localized-delocalized transition among the  $f$  electrons. Glötzel (1978) used density-functional theory to calculate the ground state properties and showed that the equation of state in the  $\alpha$ -phase can be accounted for rather satisfactorily by including the  $f$  electrons in the band structure, and furthermore that a transition to a spin-polarized state should occur at a lattice constant close to that of  $\gamma$ -Ce, though at a (negative) pressure considerably lower than that deduced from experiment. Eriksson *et al.* (1990) have recently shown that this discrepancy may be substantially reduced by including the  $l$ - $l$  coupling, which is responsible for the second of Hund's rules, in the calculation of the  $4f$  bands. This leads to a ground state in  $\gamma$ -Ce in which the  $4f$  electrons are almost fully polarized, thus occupying the Hund's-rule ground state on each site. Despite the fact that they are described in the band picture, they may thus be considered as *localized*, making very little contribution to the cohesive properties. The calculated atomic volumes in both phases are in good agreement with experiment. Podloucky and Glötzel (1983) found a cohesive energy for  $\alpha$ -Ce in accord with the measured value, while that of a 'promotional' state with no  $f$  electrons is far too small. They were also able to account for the Compton-scattering experiments of Kornstädt *et al.* (1980), who had verified that the change in  $f$  occupancy at the transition is small. Skriver (1985) calculated the crystal structure and equation of state of  $\alpha$ -Ce up to high pressures, finding very good agreement with experiment (Staun Olsen *et al.* 1985), provided that the  $f$  bands are included, but very poor agreement if the  $f$  electrons are promoted to the  $d$  bands, or are assumed to be localized, and therefore to make a negligible contribution to the electronic pressure. The relative stability at high pressures of low-symmetry configurations such as the  $\alpha$ -U structure, which is observed experimentally, is a strong indicator that there are  $f$  electrons in the conduction bands, as in the light actinides, where they play a decisive role in determining the structure (Skriver 1985).

The most powerful experimental technique available for studying the details of the electronic structure in the vicinity of the Fermi level is the de Haas–van Alphen (dHvA) effect (Shoenberg 1983), which allows a precise determination not only of the shape of the Fermi surface, but also of the effective masses of the electrons whose wave-vectors lie on it. Unfortunately, the metallurgical difficulties encountered in attempting to fabricate pure single crystals have so far precluded the observation of the effect in  $\alpha$ -Ce, but Johanson *et al.* (1981) studied the related compound CeSn<sub>3</sub>, and demonstrated that it contains itinerant  $f$  electrons of large mass at low temperatures. More recently, a number of examples of heavy-fermion Ce compounds have been investigated (Reinders *et al.* 1986; Lonzarich 1988) in which the effective masses, as deduced either from the dHvA effect or the low-temperature heat capacity, are enhanced by up to an order of magnitude compared with those deduced from band structure calculations.

There is thus very convincing evidence that the  $f$  electrons in Ce and its compounds can form bands and extend in coherent Bloch states throughout the crystal. Photoemission experiments in  $\alpha$ -Ce (Wieliczka *et al.* 1982; Mårtensson *et al.* 1982) revealed a structure with two peaks, which may plausibly be associated respectively with an itinerant  $f$  hole near the Fermi level, and one localized for a finite time at a particular ionic site (Norman *et al.* 1984; Mackintosh 1985). There are very few indications of itinerant  $f$  behaviour in the other rare earth elements, although the above-mentioned double-peaked structure is also observed in  $\gamma$ -Ce and Pr (Wieliczka *et al.* 1984), in both of which the  $f$  electrons are normally considered as localized, and as we shall see, there is evidence of an  $f$  contribution to the binding energy in some of the light rare earths. After this brief interlude, we will therefore leave the question of  $f$  bands and return to the standard model of  $f$  electrons localized on the ions, interacting with the surroundings but only indirectly with each other.

Pr, the neighbouring element to Ce, undergoes a phase transition at high pressures (Wittig 1980) which is probably associated with the formation of a band by the  $f$  electrons (Skriver 1981; Eriksson *et al.* 1990), but at ambient pressures they are localized and may be considered as part of the ionic core. Indeed, intermultiplet transitions, corresponding to those occurring on Pr ions in insulators, but shifted due to screening by the conduction electrons in the metal, have been observed by Taylor *et al.* (1988), using inelastic neutron-scattering at relatively high energies. The  $4f$  states do not therefore appear in the energy bands of Fig. 1.9, which portrays broad  $sp$  bands hybridized with a much narrower  $d$  band. As will be discussed later, Pr is paramagnetic above about 50 mK, and in zero field the Fermi surface, which is relatively complex, may be deduced from the figure to be composed of 2 electron pockets and 4 open

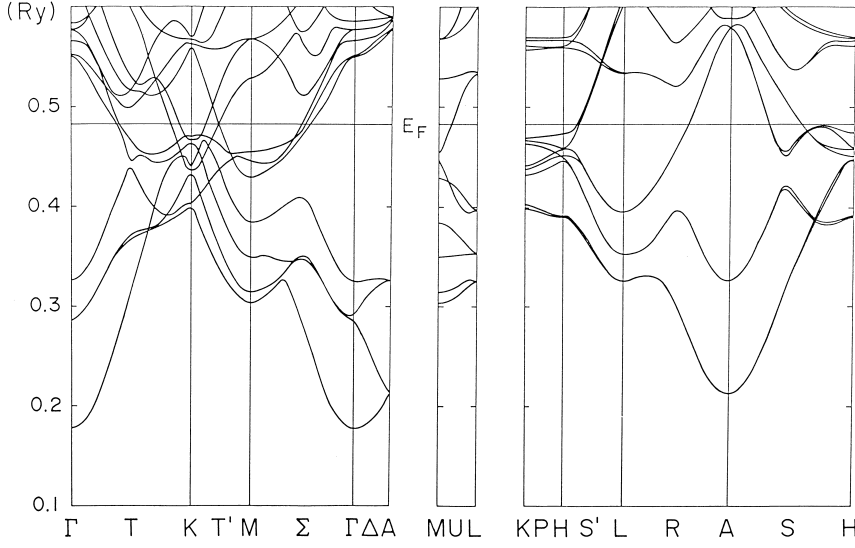


**Fig. 1.9.** The band structure of dhcp Pr, calculated by Skriver. The energy bands in the vicinity of the Fermi level are predominantly *d*-like, and the *4f* states are assumed to be localized and therefore do not appear, in contrast to Fig. 1.8.

hole sheets. However, the dHvA effect is measured in a relatively high magnetic field, and the induced moment modifies the band structure in a way which has been studied in detail by Wulff (1985). The exchange coupling between a conduction-electron spin  $s$  and the *4f* spins takes the Heisenberg form

$$\mathcal{H}_{sf} = -2Is \cdot \sum_i \mathbf{S}_i. \quad (1.3.22)$$

In the ground-state manifold, this interaction may from (1.2.29) be written

$$\mathcal{H}_{sf} = -2(g-1)Is \cdot \sum_i \mathbf{J}_i. \quad (1.3.23)$$

When a magnetic field is applied, the induced moment therefore gives rise to a splitting between the up- and down-spin energy bands. Since Pr is magnetically highly anisotropic, this splitting depends strongly on the direction of the field, but it can readily attain values of several mRy, and hence have drastic effect on the Fermi surface. In particular, the seventh-band minority-spin surface changes its topology at a critical (internal) field of about 40 kOe, as shown in Fig. 1.10,

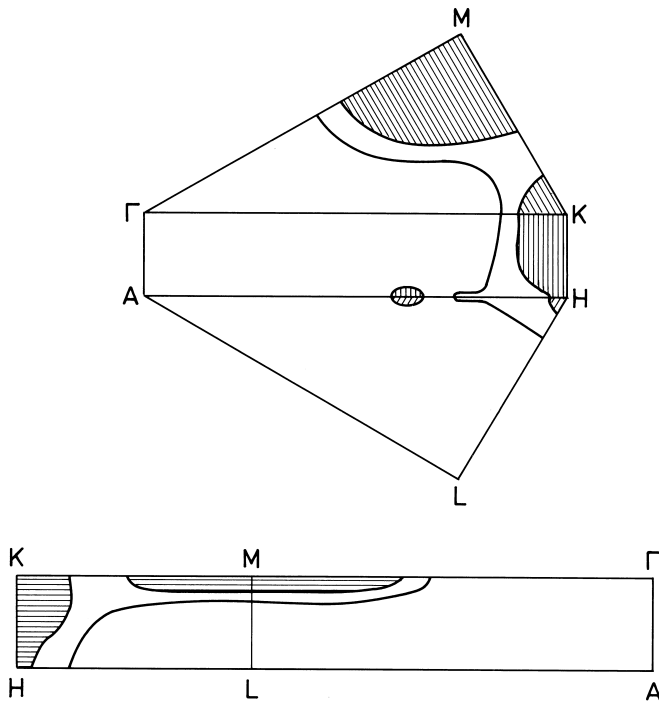


**Fig. 1.10.** The intersections of the Fermi surfaces, for the two spin states of the seventh band in dhcp Pr, with the faces of the Brillouin zone of Fig. 1.4. The surfaces are generated by a rigid splitting of the energy bands of Fig. 1.9 by 10 mRy. The unshaded majority-spin surface is a single sheet, whereas the exchange splitting modifies the topology of the shaded minority-spin surface, giving rise to a closed lens at M, a small electron pocket, and an irregular tube along HK.

and clear evidence for this transition has been observed in the dHvA effect. The changes of the Fermi surface in a magnetic field, and particularly the enhancement of the effective masses by the interaction with the  $4f$  moments (Wulff *et al.* 1988), which we will discuss further in Section 7.3, give an average value of  $I$  of about 9 mRy, with a variation of some 30% over different bands and orbits. The agreement between the measured and calculated electron orbits is such that shifts in the energy bands of only a few mRy are required to bring the two into concordance, and this is comparable to typical values for transition metals (Mackintosh and Andersen 1980). The experimental study of the dHvA effect in Pr, which is the most elaborate which has yet been undertaken for a rare earth metal, has thus led to the important conclusion that energy-band

theory gives a realistic description of the conduction electron states, and may therefore be used as a basis for the calculation of properties which depend on the electronic structure.

This conclusion could already be drawn, though with slightly less confidence, from the pioneering measurements of Mattocks and Young (1977) of the dHvA effect in ferromagnetic Gd. Because of the ferromagnetic moment, the exchange interaction (1.3.22) separates the energy bands of different spin even in zero field, and the exchange splitting is essentially independent of field. The results were interpreted in terms of the paramagnetic energy bands, originally calculated by Dimmock and Freeman (1964) and, with relativistic effects, by Keeton and Loucks (1968), taking account of the ferromagnetic structure by a rigid splitting of the bands. The resulting two majority-spin hole surfaces and the minority-spin electron surface could account for all of the observed large orbits, with a value of  $I$  close to that later deduced for Pr, and with a comparable variation through the zone. However, many small orbits were observed which could not be explained with this model, nor have subsequent band calculations, culminating in those of Temmerman and Sterne (1990), in which the exchange splitting of the conduction bands was included a priori, fully accounted for the small pieces of the Fermi surface. Although the general features of the electronic structure of Gd may therefore be considered as well understood, a further theoretical effort, taking into account the effect on the band structure of the spin-orbit coupling in the presence of both an exchange field and an external field, would be necessary to explain the finer details.

The positron-annihilation experiments of Williams and Mackintosh (1968), although at a much lower level of resolution, were also in general accord with the calculations of Keeton and Loucks (1968). They studied a number of heavy rare earths in their paramagnetic phases, showing that their Fermi surfaces are highly anisotropic and rather similar to each other. A calculation based upon energy-band theory gave a good account of the experimental results for Y. The distributions of the annihilation photons displayed a feature which is sensitive to the form of the hole surface shown in Fig. 1.11, namely the shape of the 'webbing' which may join the 'toes' on the surface near L. This characteristic is very dependent on the relative positions of the  $s$  and  $d$  bands, and the calculations indicated that the webbing is absent in Gd, very narrow in Tb, and fully developed, forming a kind of plateau, in the other heavy rare earths. These conclusions were in accordance with the positron-annihilation results, which further indicated that the webbing is destroyed in the magnetically ordered phase of Ho. The relation of these observations to the occurrence of periodic magnetic structures will be discussed in the following section.

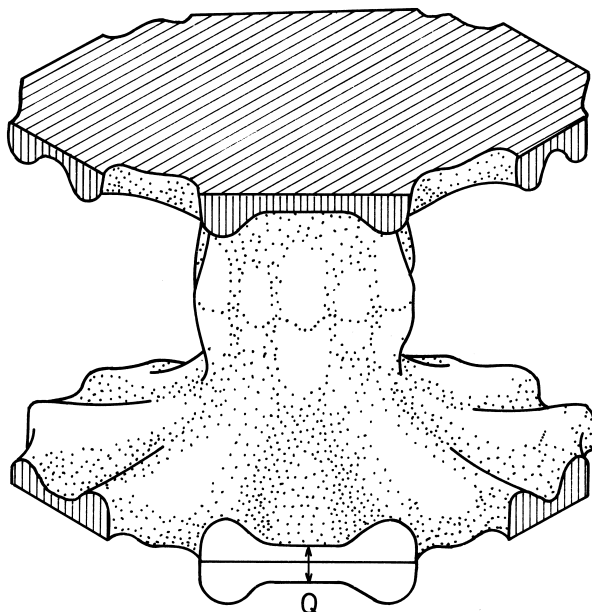


**Fig. 1.11.** The calculated hole Fermi surface of paramagnetic Tb in the Brillouin zone of Fig. 1.4. The extension of the 'webbing' between the 'toes' near the zone boundary is believed to give rise to a peak in the conduction-electron susceptibility  $\chi(\mathbf{q})$ , which determines the  $\mathbf{Q}$ -vector characterizing the helical structure.

The Fermi surface of paramagnetic Lu, in which the  $4f$  states are all filled, has also been studied by the dHvA effect (Johanson *et al.* 1982) and found to be in semi-quantitative agreement with the calculations of Tibbetts and Harmon (1982). Since the results of band structure calculations have been confirmed experimentally at the Fermi level in widely separated elements in the rare earth series, it is reasonable to suppose that they will also be successful in accounting for other ground-state properties. Characteristic band energies for the trivalent lanthanides, calculated by Skriver (1983) at a common atomic volume close to the equilibrium value for Gd, are shown in Fig. 1.12. In this figure, the effect of the change in potential is thus separated from that of the interatomic spacing. The most notable feature is the fall in energy of the  $s$  band relative to the  $d$  band with increasing atomic number, which results in a decrease of the occupation of the latter, with consequences, as we shall

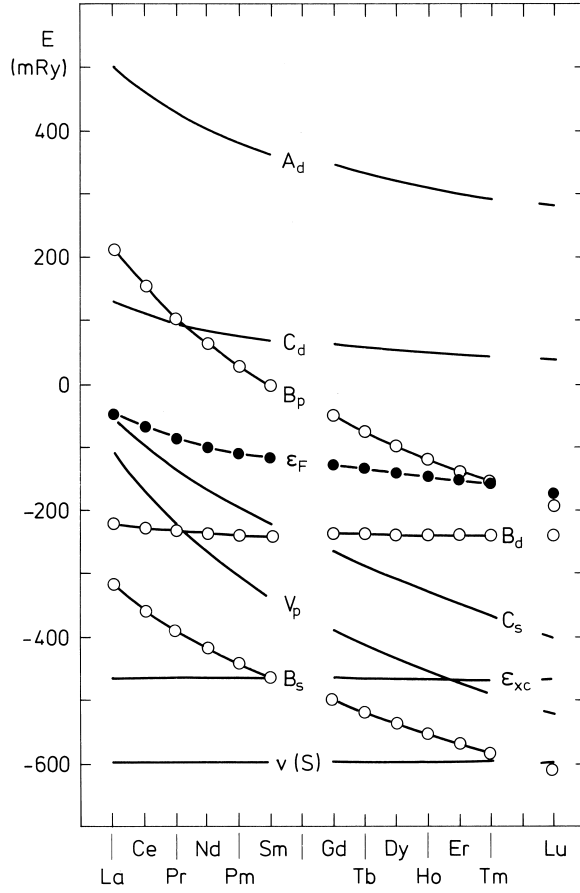


**Fig. 1.12.** Characteristic band energies for the trivalent lanthanides, for a common value of the atomic radius  $S$ , after Skriver (1983). The values of the potential  $v(S)$  and the exchange-correlation energy  $\varepsilon_{xc}$  at the atomic sphere are shown, together with the bottom,  $B_l$ , the centre,  $C_l$ , and the top,  $A_l$ , of the  $6s$ ,  $6p$ , and  $5d$  bands, and the Fermi level  $\varepsilon_F$ . The relative lowering of the  $6s$  band with increasing atomic number reduces the  $5d$  occupancy, which in turn changes the crystal structure.

see, for the crystal structure. The reason for the fall in the band energies is the increase of the nuclear charge with atomic number, which is incompletely screened by the additional  $f$  electrons. The potential  $v_{\text{eff}}(\mathbf{r})$  in (1.2.12) is therefore on average increasingly negative, and in order to maintain an unchanged boundary condition, as expressed by the logarithmic derivative, the band energies must decrease accordingly.

This effect is relatively modest for the  $d$  bands, but much greater for the  $s$  and  $p$  bands. The relative shift of the  $s$  and  $d$  bands is reduced by the adjustment of the lattice to its equilibrium configuration, but only by a small amount. As may be seen from Fig. 1.12,  $(B_d - B_s)$  increases from 101 mRy for La to 373 mRy for Lu at constant  $S$ , whereas the corresponding values for the equilibrium atomic volumes are 136 mRy and 380 mRy. The band masses also change across the series;  $\mu_d$  at constant volume increases from 2.1 in La to 3.0 in Lu, so that the  $d$  bands narrow as they fall, while  $\mu_s$  increases slightly with atomic number, but remains below 1 throughout (Skriver 1983).

The canonical-band theory may be used to calculate the electronic pressure and its partitioning between the different angular momentum components. According to the *force theorem* (see Mackintosh and Andersen 1980) the change in the total energy, due to an infinitesimal change in the lattice constant, may be determined as the difference in the band energies, calculated while maintaining the potential unchanged. We may thus write

$$dU = \delta \int^{\varepsilon_F} \varepsilon N(\varepsilon) d\varepsilon, \quad (1.3.24)$$

where  $N(\varepsilon)$  is the total electronic density of states, and  $\delta$  indicates the restricted variation with a *frozen potential*. The electronic pressure is then given by

$$\mathcal{P} = -\frac{dU}{d\Omega}, \quad (1.3.25)$$

where  $\Omega$  is the volume of the atomic polyhedron. The expression (1.3.21) for the canonical-band energies then leads to the approximate result for the  $l$  partial pressure:

$$3\mathcal{P}_l\Omega = -n_l \frac{\delta C_l}{\delta \ln S} + n_l(\bar{\varepsilon}_l - C_l) \frac{\delta \ln \mu_l S^2}{\delta \ln S}, \quad (1.3.26)$$

where  $n_l$  is the occupation number of the  $l$  states and

$$\bar{\varepsilon}_l = \frac{1}{n_l} \int^{\varepsilon_F} \varepsilon N_l(\varepsilon) d\varepsilon \quad (1.3.27)$$

is their mean energy. Equation (1.3.26) is useful for purposes of interpretation, but the results which we shall present are based upon a more accurate procedure, involving the fully hybridized self-consistent band structure (Skriver 1983).

The partial occupation numbers, state-densities and electronic pressures for  $\alpha$ -Ce, at the equilibrium lattice constant, are given in Table 1.3. The  $s$  and  $p$  electrons make a positive, repulsive contribution to

the pressure while the  $d$  and  $f$  states provide the binding, through their negative, attractive partial pressure. This difference is essentially due to the fact that the  $s$  and  $p$  wavefunctions have a positive curvature at the atomic sphere, over the energy range of the corresponding bands, as illustrated in Fig. 1.5, while the  $d$  and  $f$  functions have a negative curvature. Consequently, a decrease in volume causes an increase in the logarithmic derivative for the former and a decrease for the latter, and since  $D_l(E)$  is a decreasing function of energy, the  $s$  and  $p$  bands must rise and the  $d$  and  $f$  bands fall in order to maintain the boundary condition. Equation (1.3.25) then immediately accounts for the signs of the corresponding partial pressures. The attractive  $f$  pressure for  $\alpha$ -Ce is substantial; if it is removed, the lattice expands to a volume greater than that of  $\gamma$ -Ce. The partial pressures at a constant atomic volume for the trivalent rare earths are shown in Fig. 1.13. As may be seen, it is primarily the decrease in the  $s$  and  $p$  pressures, which has its origin in the incompletely

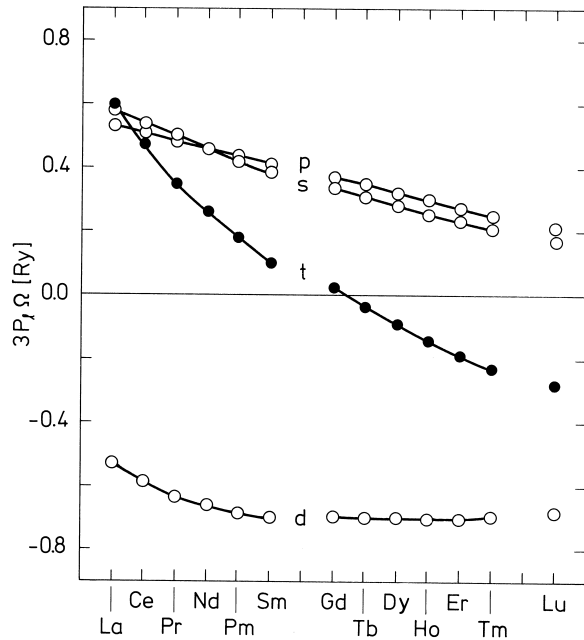


**Fig. 1.13.** The partial  $6s$ ,  $6p$ , and  $5d$  pressures for the trivalent rare earths, calculated for a common atomic volume close to the equilibrium value for Gd, after Skriver (1983). It is the decrease in the  $s$  and  $p$  pressures which gives rise to the lanthanide contraction.

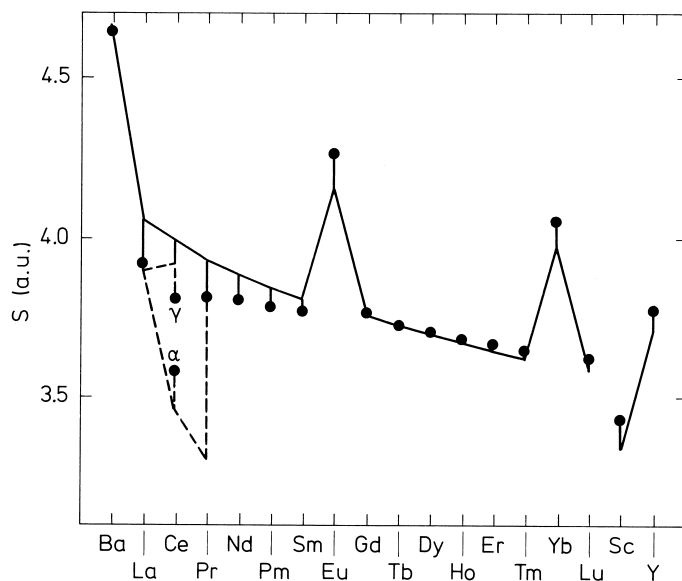


**Fig. 1.14.** The equilibrium atomic radii for the rare earth metals, after Skriver (1983). The full circles indicate the experimental values. The full line is a calculation including the  $s$ ,  $p$ , and  $d$  partial pressures, while the broken line indicates that the  $f$  contribution is also taken into account.

screened increase in the nuclear charge, which leads to the lanthanide contraction. This contraction is clearly apparent in the atomic radii shown in Fig. 1.14. The values calculated from the condition that the total pressure is zero agree very well with the experimental observations for the heavy metals, but if the  $f$  contribution is neglected, the calculated electronic pressure is increasingly too high as the atomic number decreases. As mentioned earlier, the partial pressure of the  $f$  band is essential for understanding  $\alpha$ -Ce, and it seems that the interaction of the  $f$  electrons with their surroundings makes a contribution to the binding, even in some metals in which the magnetic behaviour strongly indicates that they are localized.

In Eu and Yb, the intra-atomic interactions make it favourable to (half) fill the sub-band by transferring an electron from the conduction bands to an  $f$  state, leading to the formation of the divalent cubic structures which strongly resemble the alkaline earth metals. This transfer occurs predominantly at the expense of the  $d$  electrons, whose binding contribution to the electronic pressure is thereby reduced, causing

a substantial increase in the atomic volume. The relatively weak binding of the  $4f$  states in the divalent rare earths is clearly apparent in the experiments of Lang *et al.* (1981), who used X-ray photoemission to measure the energies required to transfer a  $4f$  electron to the Fermi level, throughout the whole series. By inverse photoemission (*Bremsstrahlung Isochromat Spectroscopy*) they were similarly able to deduce the energies required to move an electron from the Fermi level to the unoccupied  $4f$  states. Combining the two experiments, the Coulomb correlation energy required to transfer an electron from an occupied level on another site could be deduced. These energies were later calculated by Min *et al.* (1986a) using a supercell method, in which rare earth ions with different  $f$  occupancies are considered as distinct species, and the agreement with experiment was generally very satisfactory.

For close-packed structures, the atomic volume is almost independent of the structure, but there are small differences in the electronic contribution to the cohesive energy, which manifest themselves in the common structural sequence  $hcp \rightarrow dhcp \rightarrow \text{Sm-structure} \rightarrow fcc$  in the rare earths, as the atomic number is reduced or the pressure is increased. Duthie and Pettifor (1977) proposed that the  $d$ -electron occupancy,

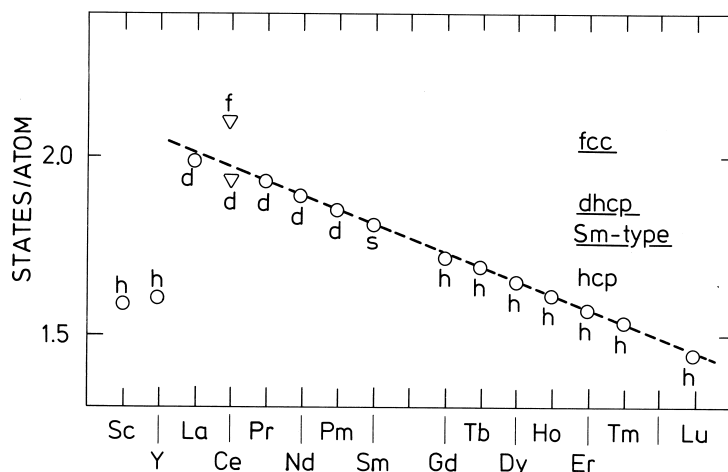


**Fig. 1.15.** The occupation numbers of the  $5d$  states for the trivalent lanthanides, at the observed equilibrium atomic volumes, after Skriver (1983). For Ce, the  $4f$  electrons are included in the energy bands. The experimentally observed crystal structures are labelled by h, s, d, and f, for hcp, Sm-structure, dhcp, and fcc, respectively. The empirical  $d$ -occupation numbers which separate the different structures are indicated by the lines on the right.

which increases through these structural sequences, is the essential determinant of the structure, and made an approximate calculation of the energy differences using canonical-band theory. The results of Skriver (1983) in Fig. 1.15 show how well the  $d$  occupancy indeed correlates with the structure. To complete the picture, Min *et al.* (1986b) demonstrated that increasing the pressure on Lu should produce a series of phase transitions following the above sequence, the first of which has been observed experimentally.

### 1.4 Magnetic interactions

In the metallic state, the  $4f$  electrons on a rare earth ion are subjected to a variety of interactions with their surroundings. These forces may be broadly classified into two categories. The *single-ion interactions* act independently at each ionic site, so that their influence on the state of the  $4f$  electrons at a particular site is unaffected by the magnetic state of its neighbours. The corresponding contribution to the Hamiltonian therefore contains sums over terms located at the ionic sites  $i$  of the crystal, but without any coupling between different ions. On the other hand, the *two-ion interactions* couple the  $4f$ -electron clouds at pairs of ions, giving terms which involve two sites  $i$  and  $j$ .

The charge distribution around an ion produces an electric field, with the local point-symmetry, which acts on the  $4f$  electrons and gives rise to the large magnetic anisotropies which are characteristic of the rare earth metals. This *crystal field* makes a contribution to the potential energy of a  $4f$  electron with charge  $-e$

$$v_{\text{cf}}(\mathbf{r}) = - \int \frac{e\rho(\mathbf{R})}{|\mathbf{r} - \mathbf{R}|} d\mathbf{R}, \quad (1.4.1)$$

where  $\rho(\mathbf{R})$  is the charge density of the surrounding electrons and nuclei. If these do not penetrate the  $4f$  charge cloud,  $v_{\text{cf}}(\mathbf{r})$  is a solution of Laplace's equation, and may be expanded in spherical harmonics as

$$v_{\text{cf}}(\mathbf{r}) = \sum_{lm} A_l^m r^l Y_{lm}(\hat{\mathbf{r}}), \quad (1.4.2)$$

where

$$A_l^m = -(-1)^m \frac{4\pi}{2l+1} \int \frac{e\rho(\mathbf{R})}{R^{l+1}} Y_{l-m}(\hat{\mathbf{R}}) d\mathbf{R}, \quad (1.4.3)$$

which is a special case of the multipole expansion (1.3.7). We can thus look upon (1.4.2) as arising from the interaction of the multipoles  $r^l Y_{lm}(\hat{\mathbf{r}})$  of the  $4f$  electrons with the appropriate components of the electric field. If part of the charge which is responsible for the crystal field lies within the  $4f$  cloud,  $v_{\text{cf}}(\mathbf{r})$  can still be expanded in spherical

harmonics with the appropriate symmetry, but the coefficients are not generally proportional to  $r^l$ , nor to (1.4.3).

As the crystal-field energy is small compared to the spin-orbit splitting, its effects on the eigenstates of the system are adequately accounted for by first-order perturbation theory. Since  $f$  electrons cannot have multipole distributions with  $l > 6$ , the properties of the spherical harmonics ensure that the corresponding matrix elements of (1.4.2) vanish. Even so, the calculation of those that remain from the electronic wavefunctions would be a formidable task, even if the surrounding charge distribution were known, if the ubiquitous Wigner-Eckart theorem did not once again come to the rescue. As first pointed out by Stevens (1952), provided that we remain within a manifold of constant  $J$ , in this case the ground-state multiplet, the matrix elements of  $v_{\text{cf}}(\mathbf{r})$  are proportional to those of operator equivalents, written in terms of the  $\mathbf{J}$  operators. We may thus replace (1.4.2) by

$$\mathcal{H}_{\text{cf}} = \sum_i \sum_{lm} A_l^m \alpha_l \langle r^l \rangle \left( \frac{2l+1}{4\pi} \right)^{1/2} \tilde{O}_{lm}(\mathbf{J}_i), \quad (1.4.4)$$

where we have also summed over the ions. The *Stevens factors*  $\alpha_l$  depend on the form of the electronic charge cloud through  $L$ ,  $S$  and  $J$ , and on  $l$ , but not on  $m$ . They are frequently denoted  $\alpha$ ,  $\beta$ , and  $\gamma$  when  $l$  is 2, 4, and 6 respectively, and their values for the magnetic rare earth ions are given in Table 1.4. The expectation value  $\langle r^l \rangle$  is an average over the  $4f$  states. The *Racah operators*  $\tilde{O}_{lm}(\mathbf{J})$  are obtained from the spherical harmonics, multiplied by  $(4\pi/2l+1)^{1/2}$ , by writing them in terms of

**Table 1.4.** Stevens factors for rare earth ions.

Ion <sup>+++</sup>	$\alpha \times 10^2$	$\beta \times 10^4$	$\gamma \times 10^6$
Ce	-5.714	63.49	0
Pr	-2.101	-7.346	60.99
Nd	-0.6428	-2.911	-37.99
Pm	0.7714	4.076	60.78
Sm	4.127	25.01	0
Tb	-1.0101	1.224	-1.121
Dy	-0.6349	-0.5920	1.035
Ho	-0.2222	-0.3330	-1.294
Er	0.2540	0.4440	2.070
Tm	1.0101	1.632	-5.606
Yb	3.175	-17.32	148.0

Cartesian coordinates and replacing  $(x, y, z)$  by  $(J_x, J_y, J_z)$ , with an appropriate symmetrization to take account of the non-commutation of the  $\mathbf{J}$  operators. They have been tabulated for  $l$ -values up to 8 by Lindgård and Danielsen (1974).

Following the customary practice, we shall generally use not the Racah operators, which are tensor operators transforming under rotations like spherical harmonics, but the *Stevens operators*  $O_l^m(\mathbf{J})$ , which transform like the real *tesseral harmonics*  $T_{lm}$ . If we define corresponding operators for  $m$  zero or positive as:

$$\begin{aligned} T_{l0} &= \tilde{O}_{l0} \\ T_{lm}^c &= \frac{1}{\sqrt{2}} [\tilde{O}_{l-m} + (-1)^m \tilde{O}_{lm}] \\ T_{lm}^s &= \frac{i}{\sqrt{2}} [\tilde{O}_{l-m} - (-1)^m \tilde{O}_{lm}], \end{aligned} \quad (1.4.5)$$

the Stevens operators for positive and negative  $m$  are proportional respectively to  $T_{lm}^c$  and  $T_{l|m|}^s$ . There is some ambiguity in the literature about the proportionality constants, but we have used the standard definitions of the Stevens operators in Table 1.5, see also Hutchings (1964). In terms of these operators, we may write the crystal-field Hamiltonian

$$\mathcal{H}_{\text{cf}} = \sum_i \sum_{lm} B_l^m O_l^m(\mathbf{J}_i). \quad (1.4.6a)$$

The *crystal-field parameters*  $B_l^m$  can in principle be calculated from the charge distribution in the metal, but in practice attempts to do so have met with limited success. The difficulties are two-fold. The charge density on the surroundings of an ion is not easy to determine with the necessary accuracy, and the approximations normally used in the calculation of the electronic structure of a metal, in particular the assumption that the charge distribution in the atomic polyhedron is spherically symmetric, are inadequate for the purpose. Furthermore, a redistribution of the charge within the cell can modify the electric fields experienced by the  $4f$  electrons, and such shielding effects are again very difficult to estimate. It is therefore necessary to appeal to relatively crude models, such as the instructive but quite unjustified point-charge model, in which an adjustable charge is placed on each lattice site, or alternatively to regard the  $B_l^m$  as parameters to be determined from experiment.

Fortunately, the number of such parameters is strongly restricted by symmetry. We shall be concerned almost exclusively with the hexagonal structures of Fig. 1.3, and in defining the Stevens operators, we have used a Cartesian system in which the  $(x, y, z)$ -directions are along the

**Table 1.5.** Stevens operators.  $X \equiv J(J+1)$  and  $J_{\pm} \equiv J_x \pm iJ_y$ .

---

$O_2^2$	$= \frac{1}{2}(J_+^2 + J_-^2)$
$O_2^1$	$= \frac{1}{2}(J_z J_x + J_x J_z)$
$O_2^0$	$= 3J_z^2 - X$
$O_2^{-1}$	$= \frac{1}{2}(J_z J_y + J_y J_z)$
$O_2^{-2}$	$= \frac{1}{2i}(J_+^2 - J_-^2)$
$O_4^4$	$= \frac{1}{2}(J_+^4 + J_-^4)$
$O_4^2$	$= \frac{1}{4}[(7J_z^2 - X - 5)(J_+^2 + J_-^2) + (J_+^2 + J_-^2)(7J_z^2 - X - 5)]$
$O_4^0$	$= 35J_z^4 - (30X - 25)J_z^2 + 3X^2 - 6X$
$O_4^{-2}$	$= \frac{1}{4i}[(7J_z^2 - X - 5)(J_+^2 - J_-^2) + (J_+^2 - J_-^2)(7J_z^2 - X - 5)]$
$O_4^{-4}$	$= \frac{1}{2i}(J_+^4 - J_-^4)$
$O_6^0$	$= 231J_z^6 - (315X - 735)J_z^4 + (105X^2 - 525X + 294)J_z^2$ $\quad\quad\quad - 5X^3 + 40X^2 - 60X$
$O_6^6$	$= \frac{1}{2}(J_+^6 + J_-^6)$

---

crystallographic  $(a, b, c)$ -axes specified in the previous section. However, it will later be convenient to rotate the  $z$ -axis into the magnetization direction, and instead orient the crystallographic  $(a, b, c)$ -axes along the  $(\xi, \eta, \zeta)$ -Cartesian directions. For an ion with hexagonal point-symmetry, as in the hcp structure or on the hexagonal sites of the dhcp structure, the crystal field is specified by 4 parameters:

$$\mathcal{H}_{\text{cf}} = \sum_i \left[ \sum_{l=2,4,6} B_l^0 O_l^0(\mathbf{J}_i) + B_6^6 O_6^6(\mathbf{J}_i) \right]. \quad (1.4.6b)$$

The Hamiltonian (1.4.6) lifts the degeneracy of the ionic  $|JM_J\rangle$  states and, since it is expressed in terms of  $\mathbf{J}$  operators, whose matrix elements between these states may be determined by straightforward calculation, it may readily be diagonalized to yield the crystal-field energies and eigenfunctions. The  $B_l^m$  may then be used as adjustable parameters to reproduce the available experimental information on these eigenstates. As an example, we show in Fig. 1.16 the splitting of the nine  $|4M_J\rangle$  states in Pr by the crystal fields acting on the hexagonal sites. This level scheme was derived from values of the crystal-field parameters adjusted

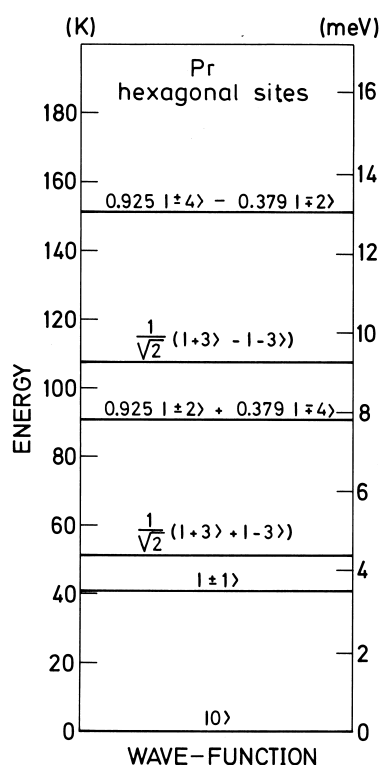


**Fig. 1.16.** The crystal-field splitting of the nine  $|4M_J\rangle$  states on the hexagonal sites in dhcp Pr. The wavefunctions are written in terms of a basis  $|M_J\rangle$  corresponding to quantization along the  $c$ -direction.

to account for a variety of experimental phenomena (Houmann *et al.* 1979).

If the lattice is strained, the crystal fields, and indeed all the other magnetic interactions which we shall discuss, are modified. In consequence, there is a *magnetoelastic coupling* between the moments and the strain, which can have profound consequences for rare earth magnetism. Magnetoelastic effects are manifested in both single-ion and two-ion terms in the Hamiltonian, though we shall mostly be concerned with the former. The elastic energy is quadratic in the strain, measured relative to the equilibrium configuration in the absence of magnetic interactions. The magnetoelastic energy is linear in the strain and the competition between the two effects may lead to some equilibrium strain or *magnetostriction*. Because of their moderate elastic constants and the large orbital component in their moments, the lanthanide metals display the largest known magnetostrictions.

Following Callen and Callen (1965), it is convenient to develop the theory in terms of the irreducible strains for hexagonal point-symmetry,

which are related to the Cartesian strains as follows:

$$\begin{aligned}
\epsilon_{\alpha 1} &= \epsilon_{11} + \epsilon_{22} + \epsilon_{33} \\
\epsilon_{\alpha 2} &= \frac{1}{3}(2\epsilon_{33} - \epsilon_{11} - \epsilon_{22}) \\
\epsilon_{\gamma 1} &= \frac{1}{2}(\epsilon_{11} - \epsilon_{22}) \\
\epsilon_{\gamma 2} &= \epsilon_{12} \\
\epsilon_{\varepsilon 1} &= \epsilon_{13} \\
\epsilon_{\varepsilon 2} &= \epsilon_{23},
\end{aligned} \tag{1.4.7}$$

where we have adopted the conventional notation of designating the Cartesian axes  $(\xi, \eta, \zeta)$  by  $(1, 2, 3)$ . The  $\alpha$ -strains are thus symmetry-conserving dilatations, the  $\gamma$ -strains distort the hexagonal symmetry of the basal plane, and the  $\varepsilon$ -strains shear the  $c$ -axis. The elastic energy may then be written

$$\begin{aligned}
\mathcal{H}_{\text{el}} = N \left[ \frac{1}{2}c_{\alpha 1}\epsilon_{\alpha 1}^2 + c_{\alpha 3}\epsilon_{\alpha 1}\epsilon_{\alpha 2} + \frac{1}{2}c_{\alpha 2}\epsilon_{\alpha 2}^2 \right. \\
\left. + \frac{1}{2}c_{\gamma}(\epsilon_{\gamma 1}^2 + \epsilon_{\gamma 2}^2) + \frac{1}{2}c_{\varepsilon}(\epsilon_{\varepsilon 1}^2 + \epsilon_{\varepsilon 2}^2) \right],
\end{aligned} \tag{1.4.8}$$

where we have defined irreducible elastic stiffness constants per ion, related to the five independent Cartesian constants by

$$\begin{aligned}
c_{\alpha 1} &= \frac{1}{9}(2c_{11} + 2c_{12} + 4c_{13} + c_{33})V/N \\
c_{\alpha 2} &= \frac{1}{2}(c_{11} + c_{12} - 4c_{13} + 2c_{33})V/N \\
c_{\alpha 3} &= \frac{1}{3}(-c_{11} - c_{12} + c_{13} + c_{33})V/N \\
c_{\gamma} &= 2(c_{11} - c_{12})V/N \\
c_{\varepsilon} &= 4c_{44}V/N.
\end{aligned} \tag{1.4.9}$$

The contributions to the single-ion magnetoelastic Hamiltonian, corresponding to the different irreducible strains, are

$$\begin{aligned}
\mathcal{H}_{\text{me}}^{\alpha} = - \sum_i \left[ \sum_{l=2,4,6} \{B_{\alpha 1}^l \epsilon_{\alpha 1} + B_{\alpha 2}^l \epsilon_{\alpha 2}\} O_l^0(\mathbf{J}_i) \right. \\
\left. + \{B_{\alpha 1}^{66} \epsilon_{\alpha 1} + B_{\alpha 2}^{66} \epsilon_{\alpha 2}\} O_6^6(\mathbf{J}_i) \right]
\end{aligned} \tag{1.4.10}$$

$$\begin{aligned}
\mathcal{H}_{\text{me}}^{\gamma} = - \sum_i \left[ \sum_{l=2,4,6} B_{\gamma 2}^l \{O_l^2(\mathbf{J}_i) \epsilon_{\gamma 1} + O_l^{-2}(\mathbf{J}_i) \epsilon_{\gamma 2}\} \right. \\
\left. + \sum_{l=4,6} B_{\gamma 4}^l \{O_l^4(\mathbf{J}_i) \epsilon_{\gamma 1} - O_l^{-4}(\mathbf{J}_i) \epsilon_{\gamma 2}\} \right]
\end{aligned} \tag{1.4.11}$$

$$\begin{aligned}
\mathcal{H}_{\text{me}}^{\varepsilon} = - \sum_i \left[ \sum_{l=2,4,6} B_{\varepsilon 1}^l \{O_l^1(\mathbf{J}_i) \epsilon_{\varepsilon 1} + O_l^{-1}(\mathbf{J}_i) \epsilon_{\varepsilon 2}\} \right. \\
\left. + B_{\varepsilon 5} \{O_6^5(\mathbf{J}_i) \epsilon_{\varepsilon 1} - O_6^{-5}(\mathbf{J}_i) \epsilon_{\varepsilon 2}\} \right].
\end{aligned} \tag{1.4.12}$$

The operators in the  $\alpha$ -strain term are the same as those in the crystal-field Hamiltonian (1.4.6b), and the associated magnetoelastic effects may thus be considered as a strain-dependent renormalization of the crystal-field parameters, except that these interactions may mediate a dynamical coupling between the magnetic excitations and the phonons. The other two terms may have the same effect, but they also modify the symmetry and, as we shall see, can therefore qualitatively influence both the magnetic structures and excitations.

It is the two-ion couplings which are primarily responsible for cooperative effects and magnetic ordering in the rare earths, and of these the most important is the *indirect exchange*, by which the moments on pairs of ions are coupled through the intermediary of the conduction electrons. The form of this coupling can be calculated straightforwardly, provided that we generalize (1.3.22) slightly to

$$\mathcal{H}_{\text{sf}}(i) = -2 \int I(\mathbf{r} - \mathbf{R}_i) \mathbf{S}_i \cdot \mathbf{s}(\mathbf{r}) d\mathbf{r} = - \int \mathbf{H}_i(\mathbf{r}) \cdot \boldsymbol{\mu}(\mathbf{r}) d\mathbf{r}, \quad (1.4.13)$$

$\mathbf{s}(\mathbf{r})$  is the conduction-electron spin density, and the exchange integral  $I(\mathbf{r} - \mathbf{R}_i)$  is determined by the overlap of the  $4f$  and conduction-electron charge clouds. This expression, whose justification and limitations will be discussed in Section 5.7, can be viewed as arising from the action of the effective inhomogeneous magnetic field

$$\mathbf{H}_i(\mathbf{r}) = \frac{1}{\mu_B} I(\mathbf{r} - \mathbf{R}_i) \mathbf{S}_i = \frac{1}{\mu_B N} \sum_{\mathbf{q}} I(\mathbf{q}) e^{i\mathbf{q} \cdot (\mathbf{r} - \mathbf{R}_i)} \mathbf{S}_i \quad (1.4.14)$$

on the conduction-electron moment density  $\boldsymbol{\mu}(\mathbf{r}) = 2\mu_B \mathbf{s}(\mathbf{r})$ . The spin at  $\mathbf{R}_i$  generates a moment at  $\mathbf{r}$ , whose Cartesian components are given by

$$\mu_{i\alpha}(\mathbf{r}) = \frac{1}{V} \sum_{\beta} \int \chi_{\alpha\beta}(\mathbf{r} - \mathbf{r}') H_{i\beta}(\mathbf{r}') d\mathbf{r}', \quad (1.4.15)$$

where  $\bar{\chi}$  is the nonlocal susceptibility tensor for the conduction electrons and  $V$  the volume. This induced moment interacts through  $\mathcal{H}_{\text{sf}}(j)$  with the spin  $\mathbf{S}_j$ , leading to a coupling

$$\mathcal{H}(ij) = -\frac{1}{V} \sum_{\alpha\beta} \iint H_{j\alpha}(\mathbf{r}) \chi_{\alpha\beta}(\mathbf{r} - \mathbf{r}') H_{i\beta}(\mathbf{r}') d\mathbf{r} d\mathbf{r}'. \quad (1.4.16)$$

If we neglect, for the moment, the spin-orbit coupling of the conduction electrons, and the crystal is unmagnetized,  $\chi_{\alpha\beta}$  becomes a scalar. The Fourier transform is:

$$\chi(\mathbf{q}) = \frac{1}{V} \int \chi(\mathbf{r}) e^{-i\mathbf{q} \cdot \mathbf{r}} d\mathbf{r} \quad (1.4.17)$$

in terms of which the integrations with respect to  $\mathbf{r}$  and  $\mathbf{r}'$  in eqn (1.4.16) are calculated straightforwardly. Summing the result over the  $N$  lattice sites, counting each interaction once only, we find that the indirect-exchange interaction takes the familiar isotropic Heisenberg form:

$$\begin{aligned}\mathcal{H}_{\text{ff}} &= -\frac{1}{2} \frac{V}{N^2 \mu_B^2} \sum_{ij} \sum_{\mathbf{q}} \chi(\mathbf{q}) I(\mathbf{q}) I(-\mathbf{q}) e^{i\mathbf{q} \cdot (\mathbf{R}_i - \mathbf{R}_j)} \mathbf{S}_i \cdot \mathbf{S}_j \\ &= -\frac{1}{2N} \sum_{\mathbf{q}} \sum_{ij} \mathcal{J}_S(\mathbf{q}) e^{i\mathbf{q} \cdot (\mathbf{R}_i - \mathbf{R}_j)} \mathbf{S}_i \cdot \mathbf{S}_j \\ &= -\frac{1}{2} \sum_{ij} \mathcal{J}_S(ij) \mathbf{S}_i \cdot \mathbf{S}_j,\end{aligned}\tag{1.4.18}$$

where

$$\mathcal{J}_S(ij) = \frac{1}{N} \sum_{\mathbf{q}} \mathcal{J}_S(\mathbf{q}) e^{i\mathbf{q} \cdot (\mathbf{R}_i - \mathbf{R}_j)}\tag{1.4.19}$$

and

$$\mathcal{J}_S(\mathbf{q}) = \sum_j \mathcal{J}_S(ij) e^{-i\mathbf{q} \cdot (\mathbf{R}_i - \mathbf{R}_j)} = \frac{V}{N \mu_B^2} |I(\mathbf{q})|^2 \chi(\mathbf{q}).\tag{1.4.20}$$

In the presence of an orbital moment, it is convenient to express (1.4.18) in terms of  $\mathbf{J}$  rather than  $\mathbf{S}$ , which we may do within the ground-state multiplet by using (1.2.29) to project  $\mathbf{S}$  on to  $\mathbf{J}$ , obtaining

$$\mathcal{H}_{\text{ff}} = -\frac{1}{2} \sum_{ij} \mathcal{J}(ij) \mathbf{J}_i \cdot \mathbf{J}_j,\tag{1.4.21}$$

with

$$\mathcal{J}(\mathbf{q}) = (g-1)^2 \left[ \mathcal{J}_S(\mathbf{q}) - \frac{1}{N} \sum_{\mathbf{q}'} \mathcal{J}_S(\mathbf{q}') \right],\tag{1.4.22}$$

where we have also subtracted the interaction of the  $i$ th moment with itself, as this term only leads to the constant contribution to the Hamiltonian;  $-\frac{1}{2}(g-1)^2 N \mathcal{J}_S(ii) J(J+1)$ . The origin of the indirect exchange in the polarization of the conduction-electron gas by the spin on one ion, and the influence of this polarization on the spin of a second ion, is apparent in the expression (1.4.20) for  $\mathcal{J}_S(\mathbf{q})$ . As we shall see, it is the Fourier transform  $[\mathcal{J}(\mathbf{q}) - \mathcal{J}(\mathbf{0})]$  which may be directly deduced from measurements of the dispersion relations for the magnetic excitations, and its experimentally determined variation with  $\mathbf{q}$  in the  $c$ -direction for the heavy rare earths is shown in Fig. 1.17.

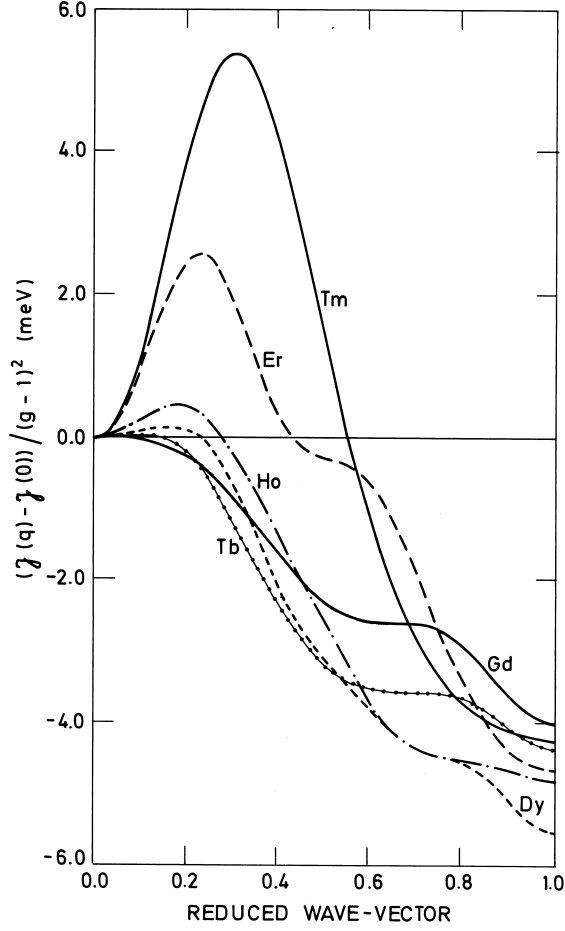


**Fig. 1.17.** The exchange interaction  $\mathcal{J}_S(\mathbf{q}) - \mathcal{J}_S(\mathbf{0})$ , determined experimentally in the magnetic heavy rare earth metals. The magnitude of the peak, which stabilizes the observed periodic magnetic structures, increases monotonically with atomic number.

A notable feature is the maximum which, except in Gd, occurs at non-zero  $\mathbf{q}$  and, as discussed in the following section, is responsible for stabilizing the periodic magnetic structures in the metals. In the approximation which we have used, the conduction-electron susceptibility is given by

$$\chi(\mathbf{q}) = \frac{2\mu_B^2}{V} \sum_{nn'\mathbf{k}} \frac{f_{n\mathbf{k}} - f_{n'\mathbf{k}-\mathbf{q}}}{\varepsilon_{n'}(\mathbf{k}-\mathbf{q}) - \varepsilon_n(\mathbf{k})}, \quad (1.4.23)$$

where  $f_{n\mathbf{k}}$  is the Fermi–Dirac function. It is clear that a large contribution to the sum is made by pairs of electronic states, separated by  $\mathbf{q}$ , one of which is occupied and the other empty, and both of which have energies very close to the Fermi level. Consequently, parallel or *nesting* regions of the Fermi surface tend to produce peaks, known as *Kohn anomalies*, at the wave-vector  $\mathbf{Q}$  which separates them, and it is believed that the parallel sections of the webbing in the hole surface of Fig. 1.11 give rise to the maxima shown in Fig. 1.17. As we have mentioned, this conjecture is supported by both positron-annihilation experiments and band structure calculations but, despite extensive efforts, first-principles estimates of  $\mathcal{J}(\mathbf{q})$  have not proved particularly successful.  $\chi(\mathbf{q})$  may be calculated quite readily from the energy bands (Liu 1978), and exhibits the expected peaks, but the exchange matrix elements which determine  $I(\mathbf{q})$  are much less tractable. Lindgård *et al.* (1975) obtained the correct general variation with  $\mathbf{q}$  for Gd, but the matrix elements were, not surprisingly, far too large when the screening of the Coulomb interaction was neglected.

The Kohn anomalies in  $\mathcal{J}(\mathbf{q})$  Fourier transform into *Friedel oscillations* in  $\mathcal{J}(\mathbf{R})$ , and such oscillations, and the extremely long range of the indirect exchange, are illustrated in the results of Houmann *et al.* (1979) for Pr in Fig. 1.18. As is also shown in this figure, they found that the *anisotropic* component of the coupling is a substantial proportion of the Heisenberg exchange. The anisotropic coupling between the moments on two ions can be written in the general form

$$\mathcal{H}_{JJ} = -\frac{1}{2} \sum_{ij} \sum_{l'l'mm'} \mathcal{K}_{ll'mm'}^{m'm'}(ij) O_l^m(\mathbf{J}_i) O_{l'}^{m'}(\mathbf{J}_j), \quad (1.4.24)$$

where the terms which appear in the sum are restricted by symmetry, but otherwise may exhibit a large variety, depending on their origin. The many possible causes of anisotropy have been summarized by Jensen *et al.* (1975). They are usually associated with the orbital component of the moment and are therefore expected to be relatively large when  $L$  is large. In addition to contributions due to the influence of the localized  $4f$  orbital moment on the conduction electrons (Kaplan and Lyons 1963), and to the magnetization and spin–orbit coupling of the latter (Levy 1969), direct multipolar interactions and two-ion magnetoelastic couplings, for which the coefficients  $\mathcal{K}_{ll'mm'}^{m'm'}$  depend explicitly on the strain, may be important. A general two-ion coupling which depends only on the dipolar moments of the  $4f$  electrons is

$$\mathcal{H}_{dd} = -\frac{1}{2} \sum_{ij} \mathcal{J}_{\alpha\beta}(ij) J_{i\alpha} J_{j\beta}. \quad (1.4.25)$$

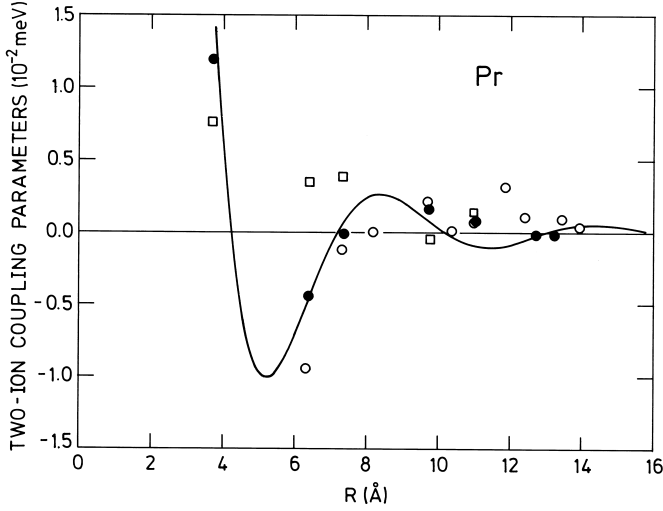


**Fig. 1.18.** The indirect-exchange interaction between ions on the hexagonal sites in Pr, deduced from measurements of the magnetic excitations at 6 K. The circles represent the isotropic interaction  $\mathcal{J}(\mathbf{R})$  between an ion at the origin and those at different sites. The filled symbols are for pairs of ions in the same hexagonal plane, and the open symbols for pairs in different planes. The former are reasonably well described by the simple free-electron model of Section 5.7.1, with an effective value of  $1.1 \text{ \AA}^{-1}$  for  $2k_F$ , as shown by the full curve. In addition, the exchange incorporates an anisotropic component  $\mathcal{K}(\mathbf{R})$ , discussed in Section 2.1.6, which is smaller, but of comparable magnitude. Its values between pairs of ions in the plane are indicated by the squares. The calculated uncertainties in the exchange interactions are, at the most, the size of the points.

The dispersion relations for the magnetic excitations provide extensive evidence for anisotropy of this form. A special case is the classical *dipole-dipole interaction* for which

$$\mathcal{J}_{\alpha\beta}(ij) = (g\mu_B)^2 \frac{3(R_{i\alpha} - R_{j\alpha})(R_{i\beta} - R_{j\beta}) - \delta_{\alpha\beta}|\mathbf{R}_i - \mathbf{R}_j|^2}{|\mathbf{R}_i - \mathbf{R}_j|^5}. \quad (1.4.26)$$

Although it is very weak, being typically one or two orders of magnitude less than the exchange between nearest neighbours, the dipole-dipole coupling is both highly anisotropic and extremely long-ranged, and may therefore have important effects on both magnetic structures and excitations. Apart from this example, the anisotropic two-ion couplings are even more difficult to calculate than are the isotropic components, so the strategy which has generally been adopted to investigate them is to

assume that all terms in (1.4.24) which are not forbidden by symmetry are present, to calculate their influence on the magnetic properties, and to determine their magnitude by judicious experiments.

The *hyperfine interaction* between the  $4f$  moment and the nuclear spin  $\mathbf{I}$  may be written

$$\mathcal{H}_{\text{hf}} = A \sum_i \mathbf{I}_i \cdot \mathbf{J}_i. \quad (1.4.27)$$

Since  $A$  is typically of the order of micro-electron-volts, the coupling to the nuclei normally has a negligible effect on the electronic magnetism in the rare earth metals, but we shall see in Sections 7.3 and 7.4 that it has a decisive influence on the low-temperature ordering in Pr.

### 1.5 Rare earth magnetism

The interactions discussed in the preceding section are the origin of the characteristic magnetic properties of the rare earth metals. The long-range and oscillatory indirect exchange gives rise to *incommensurable periodic structures*, the crystal fields and anisotropic two-ion coupling induce a *magnetic anisotropy* which may require fields up to hundreds of tesla to overcome, and the magnetoelastic interactions cause *magnetostrictive strains* which may approach one per cent. In the following, we shall give a brief description of some features of rare earth magnetism, as a prelude to a more detailed discussion of selected structures in the next chapter, and as a necessary basis for our later treatment of magnetic excitations. We have emphasized general principles, with appropriate illustrations, and have not attempted an exhaustive description of the magnetic properties of each element. This task has been accomplished by McEwen (1978), following earlier surveys by Rhyne (1972) and Coqblin (1977), and we shall refer to his comprehensive review article for further details, while quoting more recent investigations where appropriate.

Below the critical temperatures, listed in Table 1.6 on page 57, the rare earth metals form magnetically ordered phases. In the heavy elements, the maximum moment of  $g\mu_B J$  per ion is approached in moderate fields at low temperatures. As is also apparent from Table 1.6, there is an additional contribution from the conduction electrons, which is almost 10% of the total moment in Gd, and appears to fall with  $S$ , as expected from (1.3.23). In their ordered phases, all the moments in a particular plane normal to the  $c$ -axis are aligned but, as illustrated in Fig. 1.19, their relative orientations may change from plane to plane. The magnetic structures of the heavy rare earths, which have been thoroughly reviewed by Koehler (1972) and Sinha (1978), derive basically from two different configurations of moments. In the *helix*, the expectation values

of the moments take the form:

$$\begin{aligned}\langle J_{i\xi} \rangle &= \langle J_{\perp} \rangle \cos(\mathbf{Q} \cdot \mathbf{R}_i + \varphi) \\ \langle J_{i\eta} \rangle &= \langle J_{\perp} \rangle \sin(\mathbf{Q} \cdot \mathbf{R}_i + \varphi) \\ \langle J_{i\zeta} \rangle &= 0,\end{aligned}\tag{1.5.1}$$

while the *longitudinal wave*, sometimes known in the heavy rare earths as the *c-axis modulated structure* or CAM, is described by

$$\langle J_{i\zeta} \rangle = \langle J_{\parallel} \rangle \cos(\mathbf{Q} \cdot \mathbf{R}_i + \varphi),\tag{1.5.2}$$

with the two other components being zero. The wave-vectors  $\mathbf{Q}$  are along the *c*-axis, and the associated wavelength  $2\pi/Q$  does not necessarily bear any simple relationship to the lattice spacing.

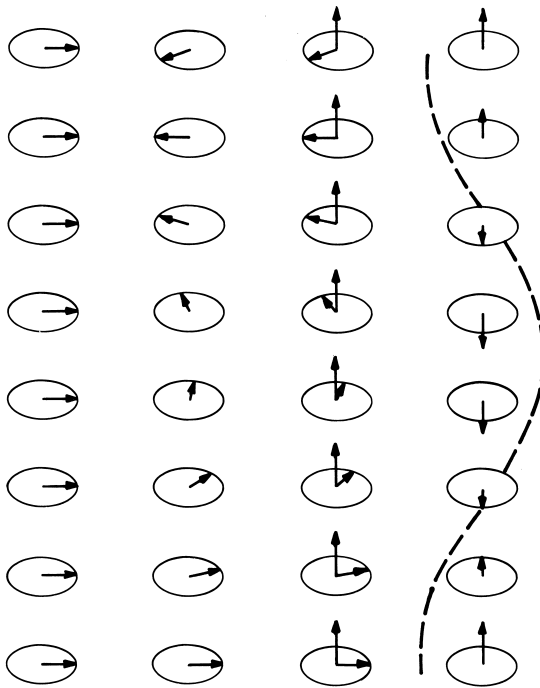


**Fig. 1.19.** Magnetic structures of the heavy rare earths. The moments in a particular hexagonal layer are parallel, and the relative alignments of different planes are illustrated. From left to right; the basal-plane ferromagnet, the helix, the cone, and the longitudinal-wave structure.

A helix is formed at the Néel temperature in Tb, Dy, and Ho, while the longitudinal-wave structure is preferred in Er and Tm. If the  $\mathbf{Q}$ -vectors are zero, a *ferromagnetic structure* results, with the ordered moment along some specified direction. In Tb and Dy at low temperatures, the easy direction of magnetization lies in the plane, while in Gd, which has a very small magnetic anisotropy, it is along the  $c$ -axis just below the Curie temperature, but is tilted about  $30^\circ$  towards the  $b$ -axis at low temperatures. If a ferromagnetic component in the  $c$ -direction is added to the helix, the moments rotate on the surface of a cone with its axis in the  $c$ -direction. This *conical structure* is stable in both Ho and Er at the lowest temperatures, but the cone angle between the  $c$ -axis and the moments at 4 K is large (about  $80^\circ$ ) in the former, and small (about  $30^\circ$ ) in the latter. If the plane of the moments in the helix is rotated about an axis in the hexagonal plane, so that its normal makes a non-zero angle with  $\mathbf{Q}$ , the structure becomes the *tilted helix*, which may be regarded as a combination of a helix and a longitudinal wave, with the same  $\mathbf{Q}$ -vectors. This structure has not been definitively identified in the elements in zero field. The moments in the hexagonal plane of Er do order below 52 K, with the same period as the  $c$ -axis modulation, but they are most probably confined to the  $a$ - $c$  plane, in an elliptically polarized *cycloidal structure* (Miwa and Yosida 1961; Nagamiya 1967) in the whole temperature interval between 52 K and the transition to the cone (Jensen 1976b). As the temperature is reduced, in the modulated  $c$ -axis phases, the moments on the individual sites approach their saturation values, resulting in a squaring of the longitudinal wave which manifests itself in higher odd harmonics. This phenomenon is observed in both Er and Tm and, in the latter, results in a low-temperature ferrimagnetic *square-wave structure* in which alternately four layers of moments point up and three layers point down.

The hexagonal anisotropy  $B_6^6$  tends to distort the helical structure, by deflecting the moments towards the nearest easy axis. In a helix which is *incommensurable* with the lattice periodicity, this effect may be treated by perturbation theory, which predicts a change of the energy in second order. However, in Ho at low temperatures,  $B_6^6$  is so large that the magnetic structure is forced to be *commensurable* with the lattice, so that  $\mathbf{Q}$  has the magnitude  $\pi/3c$ , and the turn angle between the moments in successive planes averages  $30^\circ$ . It was verified experimentally by Koehler *et al.* (1966) that, under these circumstances, the large hexagonal anisotropy causes the helix to distort so that the moments in the plane bunch about the  $b$ -directions, as illustrated in Fig. 1.20. This *bunched helix* is described by

$$\begin{aligned} \langle J_{i\xi} \rangle &= \langle J_\perp \rangle (u \sin \mathbf{Q} \cdot \mathbf{R}_i - v \sin 5\mathbf{Q} \cdot \mathbf{R}_i) \\ \langle J_{i\eta} \rangle &= \langle J_\perp \rangle (u \cos \mathbf{Q} \cdot \mathbf{R}_i + v \cos 5\mathbf{Q} \cdot \mathbf{R}_i), \end{aligned} \quad (1.5.3a)$$

where

$$u = \cos(\pi/12 - \phi) \quad ; \quad v = \sin(\pi/12 - \phi), \quad (1.5.3b)$$

and any moment deviates from the nearest  $b$ -axis by the *bunching angle*  $\phi$ . At 4 K,  $\phi$  in Ho is  $5.8^\circ$ , and it increases monotonically with temperature towards the value  $15^\circ$  which characterizes the uniform commensurable helix. An increase in temperature also causes an increase in  $Q$ , but it was shown by Gibbs *et al.* (1985) that this change does not occur smoothly and continuously. Instead, the magnetic periodicity tends to lock in to values commensurable with the lattice, and they proposed that this is a manifestation of *spin-slip structures*, in which the moments are arranged in a pattern in which one of the planes in regularly spaced members of the bunched doublets of Fig. 1.20 is omitted, while the remaining plane of the pair orients its moments along the adjacent easy axis. We shall discuss such structures in more detail in the next chapter.

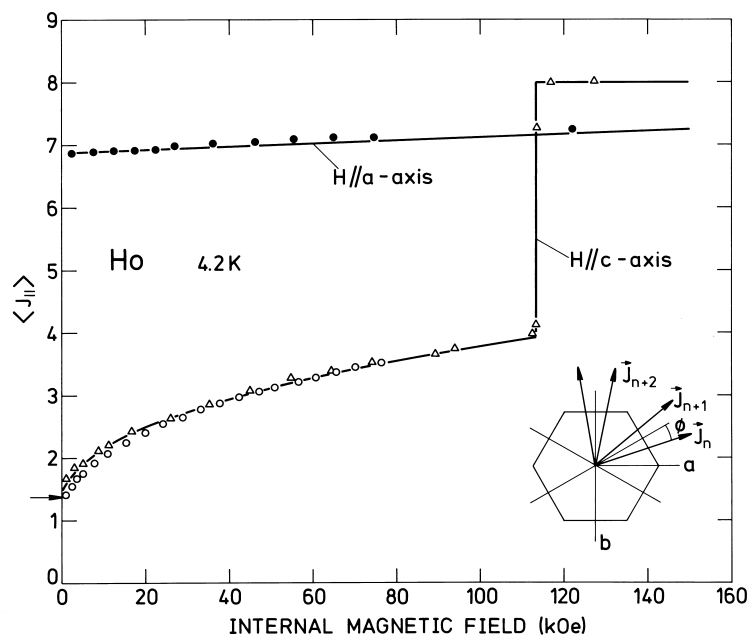


**Fig. 1.20.** The  $4f$  contribution to the magnetization of Ho at 4 K, calculated by a self-consistent mean-field theory and compared with experimental values. The zero-field structure is a bunched cone, comprising the illustrated bunched helix in the plane, and a small moment in the  $c$ -direction. The value of the  $c$ -axis moment, deduced from neutron-diffraction measurements, is indicated by the arrow.

The aforementioned magnetic structures may readily be understood as the result of the co-operation and competition between the oscillatory indirect exchange, which is relatively strong in the heavy rare earths, because  $(g-1)J$  is generally large, and the crystal-field and magnetoelastic anisotropy forces. The origin of the periodic structures can be explained by writing (1.4.21) in the form

$$\mathcal{H}_{\text{ff}} = -\frac{N}{2} \sum_{\mathbf{q}} \mathcal{J}(\mathbf{q}) \mathbf{J}(\mathbf{q}) \cdot \mathbf{J}(-\mathbf{q}), \quad (1.5.4)$$

where the Fourier transform of the magnetic structure is

$$\mathbf{J}(\mathbf{q}) = \frac{1}{N} \sum_i \mathbf{J}_i e^{-i\mathbf{q} \cdot \mathbf{R}_i}. \quad (1.5.5)$$

In order to minimize the energy of the magnetic system, this term will favour a  $\mathbf{Q}$  vector which corresponds to the maximum in  $\mathcal{J}(\mathbf{q})$ . The maxima shown in Fig. 1.17 thus reflect the observed  $\mathbf{Q}$  values in the heavy rare earths through their position, and the relative stability of the periodic structures through their magnitude. The isotropic exchange does not in itself specify any orientation of the moments relative to the crystal axes. The normal to a planar helix can, for example, be rotated into an arbitrary direction without altering the exchange energy. This flexibility is realized in Eu, where the crystal-field anisotropy is very small because, like Gd, it has no ionic orbital moment. Neutron-diffraction studies of a single crystal by Millhouse and McEwen (1973) showed a first-order transition to a helical structure, and magnetization measurements indicate that the plane of the helical structure is always normal to the direction of a moderate applied field, even though  $\mathbf{Q}$  remains along a four-fold axis of the bcc structure.

It is the magnetic anisotropy which fixes the magnetic structure relative to the crystal axes. As may be seen from eqn (1.4.4), the two-fold axial anisotropy (proportional to  $J_{\zeta}^2$ ) is also proportional to the Stevens factor  $\alpha$ . If  $A_2^0$  is negative throughout the heavy rare earths, as we shall see is the case, the values in Table 1.4 immediately explain why Tb and Dy have easy axes in the hexagonal plane, while the moments in Tm are strongly bound to the  $c$ -axis. In Ho and Er the higher-order axial anisotropy is important, but the values of  $\alpha$  are consistent with the respectively large and small cone angles. Similarly, the alternation in the sign of  $\gamma$  in the series of the heavy elements is reflected in the easy directions of magnetization in the hexagonal plane. The competition between the exchange and the anisotropy is manifested in the low-temperature magnetic structures. In the ferromagnetic phases of Tb and Dy, the

anisotropy and magnetoelastic forces, which are averaged out or ineffective in the helical structure, are strong enough to overcome the relatively weak tendency to periodic ordering. In Tm, on the other hand, a compromise obtains, by which the moments take their maximum value along the  $c$ -axis, but alternate in direction so as to take advantage of the large peak in  $\mathcal{J}(\mathbf{q})$ . In Ho, the balance is so delicate that the weak classical dipolar interaction plays a crucial role, as we shall discuss in Section 2.3.

In order to explain the temperature dependence of the structures, it is necessary to determine the configuration of the moments which minimizes the *free energy*, taking into account the influence of increasing temperature and magnetic disorder on the interactions. Provided that the magnitude  $|\langle \mathbf{J}_i \rangle|$  of the ordered moment is the same on all sites, the *entropy* term is independent of the details of the ordering (Elliott 1961), so the stable structure has the minimum *energy*. In exchange-dominated systems, like the heavy rare earths, the ordered moment approaches its saturation value at low temperature. As the temperature is increased, the structure which has the lowest energy may change as the effective interactions *renormalize*. This may occur either through a *second-order* transition, in which some *order-parameter* goes continuously to zero or, more commonly, discontinuously through a *first-order* transition. At elevated temperatures, the entropy may favour a structure, such as the longitudinal wave, in which the degree of order varies from site to site.

A conceptually simple but powerful means of calculating magnetic properties, and their dependence on the temperature, is provided by the molecular-field approximation or *mean-field theory*. We shall describe this method in some detail in the next chapter, but it is convenient to introduce it here in order to establish a few elementary results. The essential feature of the theory is the approximation of the two-ion interactions by effective single-ion terms, by replacing the instantaneous values of the  $\mathbf{J}$  operators on the surroundings of any particular ion by their thermal averages. The effect of the exchange interaction (1.4.21) with the surrounding ions on the moment at  $\mathbf{R}_i$  may then be written

$$\mathcal{H}_{\text{ff}}(i) \simeq -(\mathbf{J}_i - \frac{1}{2}\langle \mathbf{J}_i \rangle) \cdot \sum_j \mathcal{J}(ij)\langle \mathbf{J}_j \rangle, \quad (1.5.6)$$

which in turn may be written in terms of an effective magnetic field

$$\mathbf{H}_{\text{eff}}(i) = (g\mu_B)^{-1} \sum_j \mathcal{J}(ij)\langle \mathbf{J}_j \rangle, \quad (1.5.7)$$

plus a constant contribution to the energy. If the sum of the applied and effective fields is small, which will generally be true in the paramagnetic

phase (but not if spontaneous ordering occurs), the magnetic moment of the system per unit volume, neglecting the anisotropy, is given by Curie's law (1.2.32):

$$\mathbf{M} = \frac{g^2 \mu_B^2 J(J+1) N}{3k_B T} (\mathbf{H} + \mathbf{H}_{\text{eff}}). \quad (1.5.8)$$

For a uniform system, we may write

$$\mathbf{H}_{\text{eff}} = \frac{1}{g^2 \mu_B^2} \frac{V}{N} \sum_j \mathcal{J}(ij) \mathbf{M} = \frac{\mathcal{J}(\mathbf{0}) V}{g^2 \mu_B^2 N} \mathbf{M}, \quad (1.5.9)$$

recalling that

$$\mathcal{J}(\mathbf{q}) = \sum_j \mathcal{J}(ij) e^{-i\mathbf{q} \cdot (\mathbf{R}_i - \mathbf{R}_j)}, \quad (1.5.10)$$

and the susceptibility is therefore

$$\chi_{\text{MF}} = \frac{g^2 \mu_B^2 J(J+1) N}{3k_B T} \frac{1}{V} \left[ 1 - \frac{\mathcal{J}(\mathbf{0}) J(J+1)}{3k_B T} \right]^{-1} \equiv \frac{C}{T - \theta}, \quad (1.5.11)$$

where  $C$  is the Curie constant (1.2.32), and the *paramagnetic Curie temperature* is

$$\theta = \frac{\mathcal{J}(\mathbf{0}) J(J+1)}{3k_B}. \quad (1.5.12)$$

From the *Curie-Weiss law* (1.5.11) it is apparent that, if nothing else happens, the susceptibility diverges at  $\theta$ , which is therefore also the Curie temperature  $T_C$  at which spontaneous ferromagnetism occurs in this model.

The bulk magnetic properties of the rare earths are summarized in Table 1.6, where the moments are given in units of  $\mu_B$ /ion, and the temperatures in  $K$ . The theoretical paramagnetic moments per ion are  $\mu = g\{J(J+1)\}^{1/2} \mu_B$ , and are compared with values deduced from the linear magnetic susceptibilities in the paramagnetic phases, using (1.5.11). The theoretical saturation moments per ion are  $g\mu_B J$ , from (1.2.30), and are compared with low-temperature values, in fields high enough essentially to saturate the magnetization, or in the highest fields in which measurements have been made (McEwen *et al.* 1973).  $\theta_{\parallel}$  and  $\theta_{\perp}$  are the paramagnetic Curie temperatures, deduced from measurements with a field applied respectively parallel and perpendicular to the  $c$ -axis, and using (1.5.11). As we shall see in Section 2.1.1, there are corrections to this expression at finite temperatures, which give rise to a non-linearity in the inverse susceptibility. A simple linear extrapolation

therefore gives values for the paramagnetic Curie temperatures which depend on the highest temperature of the measurements. The fit to the experimental results for Tm illustrated in Fig. 2.1, for example, in which the mean-field corrections are taken into account, gives  $\theta_{\parallel}$  and  $\theta_{\perp}$  as respectively 52 K and  $-3$  K, which differ significantly from the values deduced from a linear extrapolation of the same results, given in Table 1.6. A similar analysis for Er yields 69 K and 46 K. The ordering temperatures are determined either from bulk measurements or neutron diffraction.  $T_N$  and  $T_C$  denote transition temperatures to magnetically-ordered states without and with a net moment respectively, and values are given for sites of both kinds of symmetry, in the light rare earths.

**Table 1.6.** Magnetic properties of rare earth metals.

Metal	Para. moment		Sat. moment		$\theta_{\parallel}$	$\theta_{\perp}$	$T_N$		$T_C$
	$\mu$	Obs.	$gJ$	Obs.			hex.	cub.	
Ce	2.54	2.51	2.14	0.6			13.7	12.5	
Pr	3.58	2.56	3.20	2.7 <sup>a</sup>			0.05		
Nd	3.62	3.4	3.27	2.2 <sup>a</sup>			19.9	8.2	
Pm	2.68		2.40						
Sm	0.85	1.74	0.71	0.13 <sup>a</sup>			106	14.0	
Eu	7.94	8.48	7.0	5.1 <sup>a</sup>				90.4	
Gd	7.94	7.98	7.0	7.63	317	317			293
Tb	9.72	9.77	9.0	9.34	195	239	230		220
Dy	10.65	10.83	10.0	10.33	121	169	179		89
Ho	10.61	11.2	10.0	10.34	73	88	132		20
Er	9.58	9.9	9.0	9.1	62	33	85		20
Tm	7.56	7.61	7.0	7.14	41	$-17$	58		32

<sup>a</sup> Values measured at 38 tesla.

A straightforward generalization of the above argument (see Section 2.1) gives the response of the ions in the paramagnetic phase to a spatially varying magnetic field with wave-vector  $\mathbf{q}$ . The corresponding susceptibility tensor (not to be confused with that for the conduction-electron gas) is

$$\chi_{\text{MF}}(\mathbf{q}) = \frac{g^2 \mu_B^2 J(J+1) N}{3k_B T} \frac{N}{V} \left[ 1 - \frac{\mathcal{J}(\mathbf{q}) J(J+1)}{3k_B T} \right]^{-1} = \frac{C}{T - T_N}. \quad (1.5.13)$$

Spontaneous ordering is therefore predicted to occur at the wave-vector

$\mathbf{Q}$  for which  $\mathcal{J}(\mathbf{q})$  has its maximum value, and the Néel temperature is

$$T_N = \frac{\mathcal{J}(\mathbf{Q})J(J+1)}{3k_B}. \quad (1.5.14)$$

Since, from (1.4.22),  $\mathcal{J}(\mathbf{q})$  varies as  $(g-1)^2$ , the critical temperature is expected to be proportional to the *de Gennes factor*  $(g-1)^2J(J+1)$ , provided that the susceptibility of the conduction-electron gas is constant. As may be seen from Tables 1.1 and 1.6, this relationship is rather accurately obeyed for the heavy rare earths, though not so well in the light elements. The crystal-field interactions influence the critical temperatures significantly, especially in the light end of the series, and both the electronic susceptibility and the matrix elements of the *sf*-exchange coupling, which together determine the indirect spin-spin interaction  $\mathcal{J}_S(\mathbf{q})$ , change through the series. The scaling of the critical temperature with the de Gennes factor is therefore more precise than would have been anticipated. The mean-field theory is known to be inadequate in the vicinity of the critical temperature, but as the rare earth metals are three-dimensional systems with long-range interactions, the transition temperature itself is rather well determined by this approximation. The theory is valid at high temperatures, and should describe the static magnetic structures adequately in the low-temperature limit. The discussion of the dynamical behaviour requires a time-dependent generalization of the mean-field, accomplished by the *random-phase approximation*. We shall later describe how low-temperature corrections to the mean-field properties may be derived from the magnetic-excitation spectrum, determined within the random-phase approximation. The discussion of the detailed behaviour close to the critical temperature, i.e. the *critical phenomena*, is however beyond the scope of this book, and we refer instead to the recent introduction to the subject by Collins (1989), and to the specialist literature on the application of statistical mechanics to phase transitions.

In mean-field theory, the exchange energy varies like  $\sigma^2$ , where the relative magnetization  $\sigma(T)$  is  $|\langle \mathbf{J} \rangle|/J$ . However, the anisotropy energy generally changes more rapidly with magnetization. The crystal-field parameters  $B_l^m$  in (1.4.6) are generally assumed to vary only slightly with temperature, but the thermal average  $\langle O_l^m(\mathbf{J}) \rangle$  is very dependent on the degree of ordering. By treating the deviation in the direction of the moment on a particular site from the perfectly ordered state as a random walk on a sphere, Zener (1954) showed that

$$\langle O_l^m(\mathbf{J}) \rangle_T = \langle O_l^m(\mathbf{J}) \rangle_{T=0} \sigma^{l(l+1)/2}. \quad (1.5.15)$$

We shall discuss the derivation of this thermal average by mean-field theory in Section 2.2, and show that Zener's result is indeed correct at

low temperatures. Since the anisotropy energy is very small just below the critical temperature, the exchange dominates and gives rise to periodic magnetic structures in the heavy rare earths, except in Gd where the peak in  $\mathcal{J}(\mathbf{q})$  occurs at  $\mathbf{q} = \mathbf{0}$ . As the temperature is lowered, the anisotropy forces become relatively more important, and phase transitions occur to structures in which their influence is apparent. A less obvious but nevertheless important effect is that  $\mathcal{J}(\mathbf{q})$  itself changes substantially with temperature. As was mentioned in the last section, the peak reflects a maximum in the conduction-electron  $\chi(\mathbf{q})$ , which is determined by the form of the Fermi surface. Because of the interaction (1.3.23) between the local moments and the spins of the conduction electrons, the latter experience a potential with a period which is generally different from that of the lattice, and therefore generates extra energy gaps in the band structure. These *magnetic superzone* gaps, which we shall discuss in more detail in Section 5.7, may be of the order of 10 mRy and therefore perturb the energy spectrum of the conduction electrons significantly. In particular, the regions of the Fermi surface responsible for the peak in  $\mathcal{J}(\mathbf{q})$  are severely modified, as has been verified through calculations on Tm by Watson *et al.* (1968). The result is that both the *position* of the peak is changed and its *magnitude* is reduced. As a consequence, periodic magnetic structures tend to be self-destructive; as they become established they try to eliminate the characteristic of the exchange which ensures their stability. These effects were studied by Elliott and Wedgwood (1964), who used a free-electron model to explain the variation of  $\mathbf{Q}$  in the heavy metals. Although their model is greatly over-simplified, it illustrates the essential features of the problem. We shall see in Chapters 2 and 5 that this variation in  $\mathcal{J}(\mathbf{q})$  is necessary to explain the change in both the magnetic structures and excitations with temperature.

Whereas the magnetic structures of the heavy rare earths can be accounted for by recognizing the dominant role of the exchange, and considering the crystal fields and magnetoelastic effects as perturbations, whose essential role is to establish favoured directions for the moments in the lattice, the balance in the light elements is not so clear-cut. Since  $g$  is generally close to 1, the exchange is relatively weak, and the larger values of  $\langle r^l \rangle$  towards the beginning of the series are expected to make crystal-field effects relatively important. As a result, the latter are able to hinder the moments from attaining their saturation values of  $g\mu_B J$ , even in high fields at low temperatures, as illustrated in Table 1.6.

The most remarkable manifestation of the influence of the crystal fields is found in Pr, where they are able effectively to frustrate the efforts of the exchange to produce a magnetically ordered state. As illustrated in Fig. 1.16, the ground state on the hexagonal sites is the  $|J_\zeta = 0\rangle$

singlet which, in common with all singlet states, carries no moment. The first term in (1.2.24) therefore gives no contribution to the susceptibility, but the mixing of the  $|\pm 1\rangle$  excited doublet into the ground state by the field gives a Van Vleck susceptibility at low temperatures which, if we neglect the exchange, has the form

$$\chi = \frac{2g^2\mu_B^2 M_\alpha^2 N}{\Delta V}, \quad (1.5.16)$$

where  $M_\alpha^2 = |\langle \pm 1 | J_\alpha | 0 \rangle|^2$  is the square of the matrix element of the component of  $\mathbf{J}$  in the field direction, and  $\Delta$  is the energy separation between the ground state and the first excited state. Since  $M_\alpha$  is zero when the field is applied along the  $c$ -axis, no moment is initially generated on the hexagonal sites, as confirmed by the neutron diffraction measurements of Lebeck and Rainford (1971), whereas the susceptibility in the basal plane is large. An applied field in the  $c$ -direction changes the relative energies of the crystal-field levels however, and at 4.2 K a field of 32 tesla induces a first-order *metamagnetic* transition to a phase with a large moment (McEwen *et al.* 1973), as shown in Fig. 7.13. This is believed to be due to the crossing of the ground state by the *second* excited state, as illustrated in Fig. 7.12.

If the exchange is included in the mean-field approximation, the  $\mathbf{q}$ -dependent susceptibility becomes, in analogy with (1.5.13),

$$\chi_{\text{MF}}(\mathbf{q}) = g^2\mu_B^2 \frac{N}{V} \left[ \frac{\Delta}{2M_\alpha^2} - \mathcal{J}(\mathbf{q}) \right]^{-1}. \quad (1.5.17)$$

From this expression, it is apparent that the susceptibility diverges, corresponding to spontaneous ordering, if

$$\frac{2\mathcal{J}(\mathbf{q})M_\alpha^2}{\Delta} \geq 1. \quad (1.5.18)$$

The magnetic behaviour of such a singlet ground-state system is therefore determined by the balance between the exchange and the crystal field. If the exchange is strong enough, magnetic ordering results; otherwise paramagnetism persists down to the absolute zero. In Pr, the crystal-field splitting is strong enough to preclude magnetic order, but the exchange is over 90% of that required for antiferromagnetism. We shall return to the consequences of this fine balance in Chapter 7.

The remaining close-packed light rare earths Ce, Nd, and Sm, which are amenable to experimental study (radioactive Pm is very intractable), all have an odd number of  $4f$  electrons and thus, according to *Kramers' theorem*, crystal-field levels with even degeneracy and a magnetic moment. The crystal fields cannot therefore suppress magnetic ordering,

but they reduce the ordered moment and contribute to the complexity of the magnetic structures (Sinha 1978), which is exacerbated by the two different site-symmetries in each of the metals. The magnetic structure of Ce has not been fully determined, but it now seems (Gibbons *et al.* 1987) that commensurable transverse waves are formed on both the hexagonal and cubic sites, with  $\mathbf{Q}$  in a  $b$ -direction and the moments pointing along an  $a$ -axis in the plane. The magnetic periodicity is twice that of the lattice. This relatively straightforward structure is in marked contrast to that of Nd, which displays an extraordinary complexity. An incommensurable longitudinal wave in a  $b$ -direction is formed on the hexagonal sites through a first-order transition at  $T_N$ , with a simple antiferromagnetic arrangement of successive hexagonal layers. As the temperature is lowered, a further first-order transition takes place within a degree to a double- $\mathbf{Q}$  structure (McEwen *et al.* 1985). At a still lower temperature, an incommensurable periodic structure in the  $b$ -direction is also formed on the cubic sites. At the lowest temperatures, the moments assume an elaborate quadruple- $\mathbf{Q}$  pattern (Forgan *et al.* 1989), which we shall discuss in more detail in Chapter 2. The magnetic structure on the hexagonal sites of Sm comprises pairs of planes with the moments arranged ferromagnetically in the  $c$ -direction (Koehler and Moon 1972). Adjacent pairs are coupled antiferromagnetically and separated by the cubic sites. The latter also order antiferromagnetically, with the moments along the  $c$ -axis, at low temperatures, but the normal to the ferromagnetic sheets is now in the  $b$ - $c$  plane. Although the magnetic structures of the light rare earths are phenomenologically reasonably well described, the explanation of their origin in terms of the crystal-field and exchange interactions is still at a rudimentary stage.

The application of a magnetic field adds to the Hamiltonian a term

$$\mathcal{H}_Z = -g\mu_B \sum_i \mathbf{J}_i \cdot \mathbf{H}. \quad (1.5.19)$$

In a sufficiently large field, the stable configuration is thus an array of moments  $g\mu_B J$  pointing along the field direction. The intermediate states between the zero-field structure and the high-field limit may however be very complex. In Fig. 1.20 on page 53 is shown a relatively simple example of the magnetization curves which result when a cone structure undergoes first-order transitions to the almost fully-aligned ferromagnetic state. We will discuss the effect of a magnetic field on periodic magnetic structures in some detail in Section 2.3, and therefore restrict ourselves for the moment to outlining the results of the mean-field treatment of Nagamiya *et al.* (1962) of the helical structure without planar anisotropy, to which a field is applied in the plane. The ferromagnetic

structure is reached at a field

$$H_c = \frac{J[\mathcal{J}(\mathbf{Q}) - \mathcal{J}(\mathbf{0})]}{g\mu_B}, \quad (1.5.20)$$

but there is an intermediate transition, occurring at approximately  $H_c/2$ , at which the helix transforms abruptly through a first-order transition to a *fan structure*, in which the moments make an angle  $\theta$  with the field direction, given by

$$\sin \frac{\theta_i}{2} = \left\{ \frac{2g\mu_B(H_c - H)}{J[3\mathcal{J}(\mathbf{Q}) - 2\mathcal{J}(\mathbf{0}) - \mathcal{J}(2\mathbf{Q})]} \right\}^{1/2} \sin \mathbf{Q} \cdot \mathbf{R}_i. \quad (1.5.21)$$

The opening angle of the fan thus goes continuously to zero at the second-order transition to the ferromagnetic phase.

The crystal fields manifest themselves in both microscopic and macroscopic magnetic properties. The macroscopic anisotropy parameters  $\kappa_l^m$  are defined as the coefficients in an expansion of the free energy in spherical harmonics, whose polar coordinates  $(\theta, \phi)$  specify the magnetization direction relative to the crystallographic axes. For hexagonal symmetry,

$$F(\theta, \phi) = N[\kappa_0(T) + \kappa_2^0(T)P_2(\cos \theta) + \kappa_4^0(T)P_4(\cos \theta) + \kappa_6^0(T)P_6(\cos \theta) + \kappa_6^6(T)\sin^6 \theta \cos 6\phi], \quad (1.5.22)$$

where  $P_l(\cos \theta) = (4\pi/2l + 1)^{1/2}Y_{l0}(\theta, \phi)$  are the Legendre polynomials. Anisotropic two-ion coupling and magnetoelastic strains may introduce additional higher-rank terms of the appropriate symmetry. If the Hamiltonian is written in a representation  $\mathcal{H}(\theta, \phi)$  in which the quantization axis is along the magnetization, the macroscopic and microscopic parameters are related by

$$F(\theta, \phi) = -\frac{1}{\beta} \ln \text{Tr}\{e^{-\beta\mathcal{H}(\theta, \phi)}\}. \quad (1.5.23)$$

Transforming the Stevens operators to a coordinate system with the  $z$ -axis along the magnetization direction, and assuming that the isotropic exchange is the dominant interaction, we find at absolute zero

$$\begin{aligned} \kappa_2^0(0) &= 2B_2^0J^{(2)} & \kappa_4^0(0) &= 8B_4^0J^{(4)} \\ \kappa_6^0(0) &= 16B_6^0J^{(6)} & \kappa_6^6(0) &= B_6^6J^{(6)} \end{aligned} \quad (1.5.24)$$

where

$$J^{(n)} \equiv J(J - \frac{1}{2})(J - 1) \cdots (J - \frac{n-1}{2}). \quad (1.5.25)$$

There are a number of different experimental methods for obtaining values for the microscopic and macroscopic anisotropy parameters. The susceptibility in different directions, or equivalently the torque on a crystal in a field, can be measured either in the paramagnetic or magnetically ordered phases and, as we shall discuss in detail later, much information may be obtained from the excitation spectrum and its field dependence. The values of  $\kappa_l^m(0)$  obtained from these various sources for the different elements have been reviewed and tabulated by McEwen (1978).

In order to deduce the crystal-field parameters  $B_l^m$  in the absence of exchange and magnetoelastic effects, Touborg and his collaborators studied the crystal-field states of dilute alloys of the magnetic rare earths in the non-magnetic hosts Sc, Y, and Lu, utilizing magnetization measurements and, to a limited extent, neutron spectroscopy. Their results for heavy rare earth solutes have been reviewed by Touborg (1977) and, for the light elements, by Touborg *et al.* (1978). Within the uncertainty of the measurements and of the interpretation, and with the exception of Ce in Y, which behaves anomalously, they found that a common set of parameters  $B_l^m/\alpha_l$  accounts for the behaviour of all solutes in a particular host.  $B_4^0/\beta$  and  $B_6^0/\gamma$  are roughly 10 K/ion and 15 K/ion respectively in all cases, while  $B_6^6$  is close to the value  $-\frac{77}{8}B_6^0$  which the point-charge model would predict.  $B_2^0/\alpha$  increases from about 30 K/ion in Sc, to 45 K/ion in Lu, to 100 K/ion in Y, which correlates with the deviation of the  $c/a$  ratio of the host metal (1.592 for Sc, 1.584 for Lu, and 1.573 for Y) from the ideal value of 1.633 (Orlov and Jensen 1988). It is noteworthy that the parameters  $B_l^m/\alpha_l$  show no obvious correlation with  $\langle r^l \rangle$ , as would be anticipated from (1.4.4).

The values of  $B_l^m$  from these studies of dilute alloys may be compared with those from other sources. In particular,  $B_2^0$  may be estimated for the pure metals by interpolating between the  $c/a$  ratios of the non-magnetic hosts. These values may then be compared with those deduced from the difference between the paramagnetic Curie temperatures parallel and perpendicular to the  $c$ -axis, which is shown in Section 2.1 to be given by

$$B_2^0 = \frac{5k_B(\theta_\perp - \theta_\parallel)}{6(J - \frac{1}{2})(J + \frac{3}{2})}. \quad (1.5.26)$$

The agreement for the heavy rare earths is in all cases good (McEwen 1978), indicating that the crystal fields measured in dilute alloys are related to those acting in the pure metals. On the other hand, the values deduced from torque and magnetization measurements at low temperatures in the ferromagnetic state show large discrepancies with those in the paramagnetic phase. For Tb and Dy, the former are roughly three times the latter. Despite this discrepancy, which is probably primarily

due to the anisotropic two-ion coupling in the magnetically ordered phases, the axial anisotropy parameter  $\kappa_2^0(T) - \frac{5}{2}\kappa_4^0(T) + \frac{35}{8}\kappa_6^0(T)$ , where  $\kappa_2^0(T)$  is the dominating term, depends on temperature approximately as predicted by (1.5.15), varying roughly as  $\sigma^3$  in Dy and  $\sigma^4$  in Tb. We shall return to the question of the anisotropy parameters in the rare earths when we discuss the structures and excitations.

The large magnetoelastic effects have a profound effect on the magnetic properties of the rare earths, making a significant contribution to the anisotropy, playing a decisive role in some instances in determining the structures, and modifying the excitation spectrum. We here consider for illustrative purposes a special example, the basal-plane ferromagnet, exemplified by Tb and Dy. As mentioned previously, the  $\alpha$ -strains maintain the symmetry and therefore only have the effect of renormalizing the  $B_l^m$ , and if the moments are confined to the plane, the  $\varepsilon$ -strains vanish. However, the  $\gamma$ -strains are large and symmetry-breaking, and thereby cause qualitative modifications in the magnetic behaviour. From (1.4.8) and (1.4.11), their contribution to the magnetoelastic Hamiltonian may be written

$$\mathcal{H}_\gamma = \sum_i \left[ \frac{1}{2} c_\gamma (\epsilon_{\gamma 1}^2 + \epsilon_{\gamma 2}^2) - B_{\gamma 2} \{ O_2^2(\mathbf{J}_i) \epsilon_{\gamma 1} + O_2^{-2}(\mathbf{J}_i) \epsilon_{\gamma 2} \} \right. \\ \left. - B_{\gamma 4} \{ O_4^4(\mathbf{J}_i) \epsilon_{\gamma 1} - O_4^{-4}(\mathbf{J}_i) \epsilon_{\gamma 2} \} \right], \quad (1.5.27)$$

where we have included only the lowest ranks ( $l = 2$  and  $4$  respectively) of the  $\gamma 2$  and  $\gamma 4$  terms. As shown in Section 2.2, the condition

$$\partial F / \partial \epsilon_\gamma = 0 \quad (1.5.28)$$

leads to the equilibrium strains

$$\epsilon_{\gamma 1} = \frac{1}{c_\gamma} (B_{\gamma 2} \langle O_2^2 \rangle + B_{\gamma 4} \langle O_4^4 \rangle) \\ \epsilon_{\gamma 2} = \frac{1}{c_\gamma} (B_{\gamma 2} \langle O_2^{-2} \rangle - B_{\gamma 4} \langle O_4^{-4} \rangle). \quad (1.5.29)$$

Transforming the Stevens operators as before, and using (1.5.15) to estimate the magnetization dependence of the thermal averages, we obtain

$$\epsilon_{\gamma 1} = C \cos 2\phi - \frac{1}{2} A \cos 4\phi \\ \epsilon_{\gamma 2} = C \sin 2\phi + \frac{1}{2} A \sin 4\phi, \quad (1.5.30)$$

where

$$C = \frac{1}{c_\gamma} B_{\gamma 2} J^{(2)} \sigma^3 \\ A = -\frac{2}{c_\gamma} B_{\gamma 4} J^{(4)} \sigma^{10} \quad (1.5.31)$$

are the conventional magnetostriction parameters (Mason 1954), and  $\phi$

is the angle between the  $a$ -axis and the magnetization in the plane.

The dominant contribution to the magnetoelastic energy is

$$\langle \mathcal{H}_\gamma \rangle = -\frac{1}{2} N c_\gamma (\epsilon_{\gamma 1}^2 + \epsilon_{\gamma 2}^2) = -\frac{1}{2} N c_\gamma (C^2 + \frac{1}{4} A^2 - CA \cos 6\phi). \quad (1.5.32)$$

The  $\cos 6\phi$  term makes a contribution to the hexagonal anisotropy, which is in total, from (1.5.24), (1.5.15), and (1.5.31),

$$\begin{aligned} \kappa_6^6(T) &= B_6^6 J^{(6)} \sigma^{21} + \frac{1}{2} c_\gamma C A \\ &= B_6^6 J^{(6)} \sigma^{21} - \frac{1}{c_\gamma} B_{\gamma 2} J^{(2)} B_{\gamma 4} J^{(4)} \sigma^{13}. \end{aligned} \quad (1.5.33)$$

The hexagonal anisotropy can readily be deduced from the critical field  $H_c$  necessary to rotate the moments from an easy direction to a neighbouring hard direction in the plane (respectively a  $b$ -axis and an  $a$ -axis in Tb), which is given by

$$g\mu_B J \sigma H_c = 36 |\kappa_6^6(T)|. \quad (1.5.34)$$

Values of the critical field for Tb are given as a function of  $\sigma$  in Fig. 1.21.

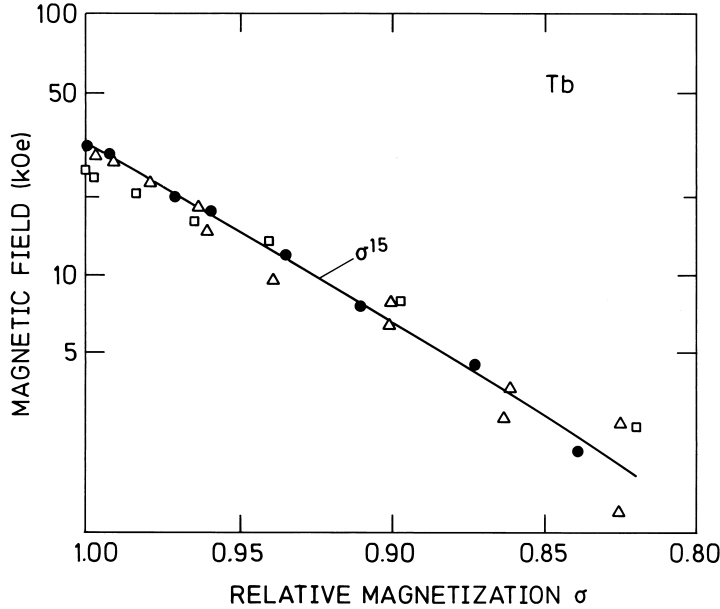


**Fig. 1.21.** The critical field  $H_c$  necessary to rotate the moments from an easy direction to a neighbouring hard direction in the plane in Tb, as a function of the reduced magnetization. The closed circles denote the results of neutron-scattering experiments, and the other signatures are deduced from macroscopic measurements.

The observed  $\sigma^{15}$  dependence on the magnetization indicates that the magnetoelastic term dominates. As illustrated in Fig. 1.22,  $C$  and  $A$  have been accurately determined by Rhyne and Legvold (1965a) from macroscopic strain-gauge measurements and, since the elastic constant is known (Jensen and Palmer 1979), the relative magnetoelastic and crystal-field contributions to (1.5.33) may readily be determined. At absolute zero, the former is 1.14 K/ion and the latter is  $-0.60$  K/ion, rapidly becoming negligible as the temperature is increased. On account of the sign of the Stevens factor  $\gamma$  for Tb, the crystal-field contribution is expected to be positive, and this may be another indication of the importance of anisotropic two-ion coupling in the magnetically ordered phases.

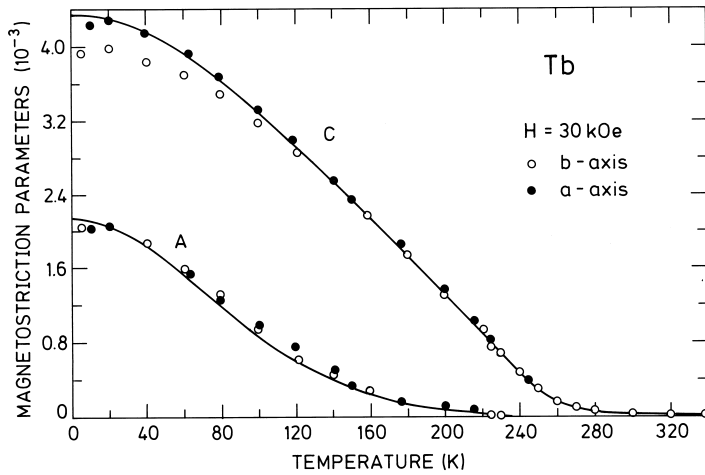


**Fig. 1.22.** The temperature dependence of the magnetostriction parameters  $C$  and  $A$  in Tb, after Rhyne and Legvold (1965a). The full lines show the results of the Callen-Callen theory presented in Section 2.2.

The magnetoelastic energy (1.5.32) is substantial in the ferromagnetic phase. In particular the term  $-\frac{1}{2}c_\gamma C^2$ , which results from a magnetoelastic strain of *cylindrical* symmetry, is relatively important at high temperatures, because it renormalizes roughly as  $\sigma^4$ , and is therefore still about 0.3 K/ion in Dy at 85 K, the temperature at which a first-order transition occurs from the helical to the ferromagnetic phase. The *hexagonally* symmetric contribution proportional to  $CA$  is small at all temperatures in Dy, since  $A \approx 0$  (Martin and Rhyne 1977). In the helical phase, the lattice is *clamped* (Evenson and Liu 1969), so that the  $\gamma$ -strains are zero, and the magnetoelastic contribution to the stabilization energy is therefore absent. At  $T_C$ , this energy, plus a minor

contribution from the crystal-field anisotropy, just balances the difference in exchange energy between the helical and ferromagnetic phases:

$$\Delta U_{\text{ff}} = -\frac{1}{2}N J^2 \sigma^2 \{ \mathcal{J}_h(\mathbf{Q}) - \mathcal{J}_f(\mathbf{0}) \}. \quad (1.5.35)$$

There has been some discussion about the relative importance of the two terms in stabilizing the ferromagnetic phase. From an analysis of the field required to induce the transition above  $T_C$ , Cooper (1968a) concluded that the magnetoelastic energy plays the dominant role. This conclusion was, however, based on the implicit assumption that the exchange energy changes little between the phases, and later measurements of the spin waves by Nicklow *et al.* (1971b) demonstrated that this is not the case. The energy difference  $-\frac{1}{2}J^2\sigma^2\{\mathcal{J}_h(\mathbf{Q}) - \mathcal{J}_h(\mathbf{0})\}$  is about 2 K/ion in the helical phase, but the corresponding quantity is substantially smaller in the ferromagnetic phase. Del Moral and Lee (1975) reanalysed the data and concluded that the change (1.5.35) in the exchange energy makes the major contribution to driving the transition. Any statement about what drives a *first-order*, as distinct from a *second-order* transition must necessarily be imprecise, since all contributions to the energy change discontinuously at the transition. Immediately below  $T_N$ , the exchange dominates and the anisotropy forces are small. As the temperature is lowered, the peak in  $\mathcal{J}(\mathbf{Q})$  decreases and moves, as was shown explicitly for the analogous case of Tb by the spin-wave measurements of Bjerrum Møller *et al.* (1967), illustrated in Fig. 6.1. The magnetoelastic forces therefore increase in relative importance, until a balance is reached and the transition to the ferromagnetic phase takes place. At the transition, a large change occurs in the exchange. Without the magnetoelastic term,  $T_C$  would be determined by the hexagonal crystal-field anisotropy, and would therefore be much lower. In this sense, the cylindrically-symmetric magnetoelastic forces drive the transition.